University of Louisville

ThinkIR: The University of Louisville's Institutional Repository

5-2016

Mixing and mean age in multiphase systems.

David Chandler Russ
University of Louisville

MIXING AND MEAN AGE IN MULTIPHASE SYSTEMS

By

David Chandler Russ
B.S., University of Louisville, 2010
M.Eng., University of Louisville, 2011

A Dissertation
Submitted to the Faculty of the
J.B. Speed School of Engineering
of the University of Louisville
in Partial Fulfillment of the
Requirements for the Degree of

Doctor of Philosophy
in Chemical Engineering

Department of Chemical Engineering
University of Louisville
Louisville, Kentucky

May 2016

MIXING AND MEAN AGE IN MULTIPHASE SYSTEMS

By

David Chandler Russ
B.S., University of Louisville, 2010
M.Eng., University of Louisville, 2011

A Dissertation Approved on

January 26, 2016

by the following Dissertation Committee:

_____
R. Eric Berson (Dissertation Director)

_____
Gerold Willing

_____
Xiao-An Fu

_____
Yongsheng Lian

DEDICATION

This dissertation is devoted to my wife

Mrs. Deandra Leigh Russ

whose love and support for me have been immeasurable, and our daughter

Miss Eliora Kathryn Russ

who is my pride and joy.

ACKNOWLEDGEMENTS

I would like to thank my advisor, Dr. Eric Berson, for many years of patience and guidance. I would also like to thank the rest of my committee, Dr. Jerry Willing, Dr. Sean Fu and Dr. Yongsheng Lian, for their willingness to serve on my dissertation committee. I would like to thank my wife Deandra for always encouraging me to push forward and for being willing to make personal sacrifice to ensure my success. I would also like to thank my parents, Bill & Carol Russ, as well as my brother and his wife, Mark & Lauren Russ, for their support and encouragement.

ABSTRACT

MIXING AND MEAN AGE IN MULTIPHASE SYSTEMS

David Chandler Russ

January 26, 2016

Mean age theory is a useful tool for analyzing mixing by providing spatial distributions of time based data for material inside a system using a steady-state CFD approach, but has been limited to single phase systems. Mean age theory was extended here to multiphase systems by defining the scalar tracer concentration independently for individual phases, which allows mean age to be solved at steady-state for each phase independently within a multiphase system. The theory was validated by comparing multiphase mean age (MMA) distributions extracted from spatial distributions determined computationally at two locations where RTDs were experimentally measured in a water-oil flow system. Mean residence times from MMA theory were within 1-3% of experimental values and variances were within 3-11%.

MMA was then modified for applicability to closed systems and applied towards predicting just suspended speed in mixing tanks by evaluating MMA near the bottom surface through strategic zone selection. MMA equations were solved only in a thin section along the bottom of the vessel (~1% of the vessel height), allowing the mean age in proximity to the bottom to be computed. The technique was accurate within 1-3% of experimental values across a range of solid densities, solid fractions, and particle sizes while using multiple impeller types and vessel geometries.

At high-solids conditions, biomass slurries exhibit non-Newtonian single phase behavior with a yield stress and require high power input for mixing. The goals was to determine the effect of scale and geometry on power number, P0, and estimate the power for mixing a biomass slurry in a million gallon hydrolysis reactor of conventional design. A lab-scale CFD model was validated against experimental data and then scaled up. A pitched-blade turbine and A310 hydrofoil were tested for various geometric arrangements. Flow was transitional; laminar and turbulence models resulted in equivalent P0 which increased with scale. The ratio of impeller diameter to tank diameter affected P0 for both impellers, but impeller clearance to tank diameter affected P0 only for the A310. At least 2 MW is required to operate at this scale.

TABLE OF CONTENTS

LIST OF FIGURES

CHAPTER 1. INTRODUCTION

Residence-time distributions (RTD) are a key indicator of degree of mixing in continuous processes. The concept of residence time typically refers to material exiting the system, but in some cases local residence times are described within a system. The concept of age typically only refers to materials inside the system and can provide additional information regarding internal distribution above and beyond just the typical RTD's. Complete spatial distributions of mean age provide the most value, but are generally impractical to develop experimentally since sampling and measurement is required across an entire system volume. Measuring residence times (or age) require tracking the movement of a passive tracer, such as through the use of a flammable gas in air (Baleo and Cloirec, 2000), radioactive isotope (Sinusas et al., 2014) or an appropriately defined chemical reaction (Liu and Tilton, 2010).

A highly innovative approach to mixing research in recent years has been towards application of mean age theory (Baleo & Cloirec, 2000; Liu & Tilton, 2010), which was originally proposed by Danckwerts (1958), although in 1958 the lack of computing power made the proposition purely theoretical and not practical. Mean age theory allows for redefining time as a passive scalar variable in the advection-diffusion equation, which then allows for analysis of traditionally time based variables, such as mean residence time or mixing time (Liu, 2011c), while using *a steady-state* solution. Conventional solutions to the advection-diffusion equation required a time-demanding, computationally intensive transient solution, particularly when additional complications were introduced such as multiple phases, non-Newtonian flow, and turbulence. Even when a solution at steady-state is desired, the transient calculation is still necessary for modeling the time dependent tracer behavior. Computational Fluid Dynamics (CFD) solutions of mean age are additionally beneficial since (i) they can provide spatial and

temporal resolution within the flow field, (ii) provide insight above conventional velocity vector and contour plots, and (iii) provide solutions when traditional experimental measurements are difficult or not possible (Sarkar, 2014).

Mean age theory has not yet been applied to multiphase systems. Mean age theory extended to multiphase systems by defining the scalar tracer concentration independently for individual phases, would allow mean age to be solved at steady-state for each phase independently within a multiphase system. A new technique applicable to multiphase systems would extend the usefulness to a larger, and arguably more important, classification of processes. The steady-state form of the advection-diffusion equation is not limiting in terms of the magnitude of age, or residence time, and therefore allows for solutions of extraordinarily long time-scale applications, on the order of days, months, and years, that are currently impractical, and improve the computational efficiency for others. Example applications that would benefit include pollution modeling (Samano et al, 2014), fluidized beds (Patil et al, 2003), sedimentation in surface water (Wang et al, 2013), and cardiovascular applications (Tambasco & Steinman, 2002).

One of the major benefits to mean age theory is the ability to collect time-related data throughout a spatial distribution. This allows for focusing on specific regions in a vessel, either closed or continuous, rather than focusing on the overall distribution from inlet to outlet. One particular application where mean age is of interest in a confined region is solids settling in liquid-solid suspension systems. In this case, the behavior of the solids at or near the tank bottom is most relevant. The most common time-based mixing metric that relates to solids suspension near the tank bottom is just suspended speed (N_{jss}). In most solid-liquid systems, suspension of the solid particle is essential to maintaining adequate mass transfer. The particle resting on the bottom of the tank does not have its entire surface area exposed, and thus mass transfer between the solid and liquid phases is inhibited. Much research has focused on determining just suspended speed (N_{jss}), the minimum impeller speed necessary for all solid particles to maintain

off-bottom suspension. Numerous methods have been proposed to determine just suspended speed, but no method is universally accurate and applicable. Many experimental techniques require lower solids fractions or a transparent system for measurement, while others involve intrusive sensors.

Since N_{jss} is a time-based metric, it can be analyzed with multiphase mean age theory. N_{jss} is a measure of how long solids remain in proximity to the vessel bottom, so a method defining age elapsed in a zone near the bottom, rather than from the vessel inlet, could help accurately determine N_{jss} through steady state CFD.

When solids loading becomes high enough, solid particles are not free to move independently of each other. High solids slurries can have complicated rheology, and they can appear to behave similarly to non-Newtonian fluids. Power requirements become a significant factor in these highly viscous systems. Factors such as scale or solids loading can significantly change the minimum power requirements to maintain adequate agitation, and these factors are not always linearly related. Scale will change how the shear is propagated throughout the vessel, which in turn will impact the location and intensity of turbulence. High solids loading can impact the rheology of the fluid, which in turn will impact how shear is propagated throughout the vessel and the corresponding turbulent intensity. In the latter case, modeling rheology is the first critical step to predicting power requirements.

One example of this sort of problem is mixing in enzymatic hydrolysis reactors. Enzymatic hydrolysis of lignocellulose requires days to reach a high yield. While intense mixing may not be necessary due to the slow reaction, a certain amount is required to overcome bulk mass transfer limitations, especially at high solids loading, to disperse enzymes and carry products away from reaction sites. Higher solids concentration is desirable in order to yield a larger concentration of sugar from the reaction, decrease water and energy usage, and reduce the size necessary for reactor vessels, provided the reaction rate can be maintained at high solids

loads. However, achieving adequate mixing can be difficult for highly viscous, non-Newtonian rheology, which is characteristic of biomass slurries.

Non-Newtonian biomass slurries are highly viscous, which can make power consumption a major concern when scaling up to industrial scales. Further, these systems are often reported as having shear-dependent rheology and yield stresses. Changing solids loading by 5% can have an order of magnitude change in the apparent viscosity, with non-newtonian behavior increasing significantly. The highly viscous, shear dependent nature of the slurry makes mixing more difficult. Viscosity is non-uniform throughout the tank, meaning that energy and shear are more localized around the impeller. This can cause dead zones (regions of unyielded material) in sections of the vessel. Further, this makes achieving a fully turbulent condition prohibitively difficult or impossible. High intensity mixing will usually be transitional, with some regions turbulent, others laminar. Predicting mixing and power draw in these systems is system-dependent. In turbulent conditions, impeller power number is considered constant with scale or viscosity, but prediction of power number in the transition regime is much less certain. The non-Newtonian rheology makes prediction of power number more difficult. It is currently unknown how scale effects power number in non-Newtonian systems.

1.1. Objectives

1. Develop a computational steady-state method for determining mean age distributions of individual phases in multiphase systems, and validate the method against both experimental data and conventional transient solutions.

2. Apply the multiphase mean age technique towards a novel approach for predicting just suspended speed by obtaining local, time dependent data for solids in proximity to the bottom of mixing vessels.

3. Evaluate the effect of scale and rheology on dimensionless power number in high solids biomass slurries

CHAPTER 2. LITERATURE REVIEW

2.1 Residence time and age

Mean age and residence times as concepts trace their earliest roots to Dankwerts (1953). Prior to Danckwerts, mixing in a vessel was approximated as either plug flow (no mixing), or else as an ideal CSTR (perfect mixing). In 1953 Danckwerts mathematically demonstrated the value in modelling real mixing processes by measuring the amount of time spent in the vessel through the residence time distribution function. He tested this concept in packed bed flow, pipeline flow and flow through a stirred tank. He was able to substantially demonstrate the RTD as an effective means of quantifying mixing in a real vessel.

Later, Danckwerts (1958) extended the concept of residence time distributions to anywhere in a vessel. He called this new value 'age,' with the age at the outlet being equal to the residence time. The local age distribution could be determined through local measurement, though it was not attempted in this article. Nonetheless, this became a useful concept.

Spalding (1958) provided much of the groundwork required for deriving a transport equation for mean age (the first moment of age). He presented the definition for mean age:

$$a(x) = \frac{\int_0^\infty tC(x,t)\,dt}{\int_0^\infty C(x,t)\,dt}$$ (1)

where C is the concentration of a hypothetical scalar at some location x and some time t. Sandberg (1981) followed Spalding's derivation and brought it to its conclusion – a transport equation for mean age which is based on the advective-diffusive equation:

$$\frac{\partial C}{\partial t} + \nabla \cdot (uC) = \nabla \cdot (D\nabla C)$$ (2)

Modifying this equation with the definition of mean age and the recognition that age and time are related leads to the conclusion:

$$u\nabla a = \nabla \cdot D\nabla a + 1$$ (3)

This final equation provides the transport for mean age, rather than concentration of a scalar. Of note is the fact that the unsteady term as been replaced by a scalar constant source term. This is intuitive, in that one unit of mean age should be produced for every unit of time elapsed.

The boundary conditions were shown to be the same as those for the concentration:

$a = 0$ Inlet (4)

$\dfrac{\partial a}{\partial x_n} = 0$ Outlet (5)

$\dfrac{\partial a}{\partial x_n} = 0$ Wall (6)

Baleo and le Cloirec (2000) provided experimental validation for the mean age transport equation in CFD. They designed a model system with turbulent flow through a pipeline. The main flow was air, and the tracer was butane. The pipeline contained several sudden expansions, followed by corresponding contractions. This geometry

created recirculation loops in the expanded region. When they measured the mean age at several positions in the pipe, both computationally and experimentally, they found agreement within 5%. Thus this work validates the use of the mean age transport equations for computationally determining the spatial distribution of mean age.

2.2 Applications of mean age

Liu and Tilton (2010) introduced the concept of higher moments of age. If age has a distribution function, the first moment (mean age) is related to the mean of that function. The second moment relates to the variance, and the third moment relates to the skewness of the age distribution function. This paper highlighted the advantage of mean age calculation by emphasizing the spatial distributions which can be obtained from the CFD results. The most groundbreaking contribution of this paper however was its influence in renewing the interest in mean age amongst mixing applications.

Liu (2011a) applied mean age theory towards calculating the degree of mixing in a generic continuous flow field. Degree of mixing is a method for quantifying mixing that was originally proposed by Danckwerts, and later developed by Zwietering, but without the use of CFD, it is a technique that has not received much use. Liu's method combines the spatial distribution of the mean age with that of the second moment of age (which is related to the variance of age). He proposed the degree of mixing parameter would be especially useful for analyzing non-deal stirred tank reactors.

Liu (2011b) also applied mean age theory towards modeling tracer concentrations in a stirred tank reactor. Tracer concentrations is a standard technique used experimentally, and it is often used in unsteady state CFD simulations, but by effectively modeling it through a steady state mean age technique, Liu significantly reduced the

computational cost required to use this metric to analyze mixing quality. This steady state work was validated against unsteady CFD data.

Liu (2011c) applied mean age theory to measuring blend time in stirred tanks. Blend time is a metric commonly used in single phase mixing and less commonly in multiphase mixing to describe the amount of time required to achieve a certain degree of homogeneity within a vessel, generally 99%. Liu's method requires the use of an open system, but for closed systems he specified an inlet and outlet flow rate to be arbitrarily low. If the blend time is much shorter than the mean residence time, the technically open system should give the same results as a true closed system, but it is still an approximation.

Liu (2012a) expanded upon his work on the relationship between mean age theory and degree of mixing. In this paper, he derives the relationship between the higher moments of age to the moments of residence time. Using this, he is able to use mean age to calculate the degree of mixing for non-ideal CSTRs. Thus Liu significantly improves researchers' abilities to analyze the mixing quality in real vessels through the use of mean age theory and steady state CFD.

2.3 Residence time distributions in multiphase systems

Data relating residence time distributions to individual phases in a multiphase system are limited. In well mixed systems, there should not be much deviation between the residence time distributions for the separate phases, as opposed to the distribution for the mixture. Experimentally, the tracers for each phase must be selected carefully to ensure there is no transfer from one phase to another.

Barigou et al (2003) performed exactly this sort of experiment when modelling a food sterilization process. Using positron emission tracking, this study was able to determine transit time distributions between two measuring points for small and large particles. They found that the small particles moved significantly faster than the large. This study provides a proof of concept for measuring residence time distributions for independent phases in a multiphase system.

Sugiharto (et al, 2009) studied the residence time distributions for water and oil in three phase flow (liquid-liquid-gas). Their results showed the water phase traveling a 100m section of pipe significantly faster than the oil phase. Further, the oil phase had a broader residence time distribution, indicating more mixing in the secondary phase. This study is very rare in that it not only measured residence time distributions for independent phases, but directly compared them together within the same system, allowing for analysis of the relative flow behavior in each phase.

2.4 Just suspended speed

In many liquid-solid systems, wetted surface area is a key condition for process rate. When solids have settled to the bottom of the vessel, the wetted surface area is diminished, lowering the rate of reaction, dissolution, etc. Conversely, if there are other rate limitations involved, then once complete off-bottom suspension has been obtained, additional agitation will not significantly affect the process rate, and therefore is wasted power. Thus this concept of complete off-bottom suspension is related to both mixing quality and power requirement.

Zwietering (1958) first proposed the concept of complete off-bottom suspension as a key design metric for liquid-solid mixing. He studied thousands of different

9

combinations of liquid and solid densities, solids loading, particle sizes and system geometries. By slowly adjusting the impeller speed, he was able to determine the precise point at which complete off-bottom suspension occurs, which he termed just suspended speed (N_{jss}). Just suspended speed was obtained when no solid particle could be observed remaining on the tank bottom for more than 1-2s. He also developed a correlation based on his data for predicting just suspended speed:

$$N_{jss} = S \left(\frac{g(\rho_s - \rho_l)d_p}{\rho_l} \right)^{0.45} \left(\frac{v^{0.1}X^{0.13}}{d_p^{0.25}D^{0.85}} \right) \tag{7}$$

where g is gravitational acceleration, ρ is density, d_p is the particle diameter, v is the kinematic viscosity of the fluid, X is the mass ratio of the solids to the liquid, D is the impeller diameter, and the subscripts s and l indicate the solid and liquid phase, respectively. S is an empirical geometric constant based on impeller type, size and location. This method and the resulting correlation are still widely used today, and is considered the gold standard for experimental measurement of N_{jss}. Even though it is subjective (dependent on the observer, 1-2s range), Zwietering suggested with an experienced observer, observations were reproducible to within 2-3%. There are, however, significant drawbacks to this method. Most significantly, the method cannot be used when visibility is hindered. Opaque suspensions, high solids volume fractions and opaque tanks all render the method unworkable. Consequently, the method is useful only within a narrow range of laboratory conditions; outside of these, the method breaks down.

Einenkel & Mersmann (1977) proposed a method for determining just suspended speed based on measurements of the cloud height. In a liquid-solid system, cloud height is a measure of the maximum height at which solids are suspended. Above the cloud is a

single phase, liquid system, while in the cloud is the two phase region. Einenkel's method showed high accuracy, but this method is still highly limited. Any system which has a dispersion of particle properties will potentially have a uniform suspension of the smaller or lighter particle, while the heavier or larger particle will not be completely suspended.

Musil & Vik (1978) proposed a method based on solids concentration near the bottom of the vessel. As impeller speed increases, more particles are suspended higher in the vessel. As the impeller speed approaches just suspended speed, the concentration of solids on the bottom will exhibit a sharp, discontinuous drop, as previously unsuspended solids are suddenly entrained in the flow. This method shows relatively high accuracy, but it requires the use of an intrusive sensor, which can impact the flow field (and the just suspended speed). Further, accurate measurement of solids concentration can be difficult depending on the nature of the solids.

Chapman (et al, 1983) proposed a similar method to Musil's. Rather than seek the discontinuity in solids concentration on the vessel bottom, Chapman proposed looking for the peak in concentration a little above the tank bottom. At just suspended speed, a large amount of solids will suddenly suspend, but will not be uniformly suspended. Chapman's method recognizes that at impeller speeds slightly above just suspended speed, most of those freshly suspended solids will still congregate near the bottom. This method has the same major drawbacks as Musil's, in that it requires an intrusive sensor and measuring solids concentration can be difficult in some circumstances.

Buurman et al (1986) suggested a method for determining just suspended speed by measuring relative velocity of solids near the bottom. Buurman set up a Doppler sensor at the bottom of a mixing tank and found that the local velocity of the solids could be determined. Since below just suspended speed there will be significant solids that have no vertical velocity, this method could identify the transition to suspension. This method never obtained widespread use, however, as the sensor apparatus can be interfered with by the tank wall, and placing the sensor inside the tank would create the same problems with an intrusive sensor as Chapman's and Musil's methods.

Micale et al (2002) proposed measuring the static pressure at the vessel bottom as a means of detecting just suspended speed. As the solids suspend, there will be a measurable drop in the static pressure along the bottom. The drawbacks to this method are the difficulty of separating the static and dynamic components of pressure, as well as the high sensitivity to the location of the pressure sensor.

Of all the many studies published regarding measuring, predicting or applying just suspended speed, Zwietering's remains the most influential. Jafari et al (2012) published a comprehensive literature review of just suspended speed in liquid-solid systems. His analysis indicates that Zwietering's method is still used in the vast majority of just suspended speed studies, and virtually all the published correlations for predicting are modified forms of Zwietering's original correlation. The few CFD studies on just suspended speed are limited in their ingenuity as well, in that they either replicate existing experimental techniques, or else use particle tracking to simulate the motion of actual particles to determine if they are held up at the bottom (Jafari et al, 2012). Bashiri et al (2011) systematically compared CFD results with experimental in turbulent

conditions and found that these models can still generate errors as high as 20%. A new, accurate CFD technique would be a welcome addition to the field.

2.5 Mixing power

Mixing cost is primarily related to power consumption. While power is easy to measure, it is often more difficult to predict, especially with non-Newtonian rheology and multiple scales. In 2002, the US National Renewable Energy Laboratory (NREL) set a goal for a 975,000 gal enzymatic hydrolysis process with the end goal of producing bioethanol for fuel use (Aden et al, 2002). The feedstock was to be a lignocellulosic slurry, specifically pretreated corn stover. This is an agricultural byproduct. Intense mixing is not necessary due to the slow enzymatic reaction. Minimal agitation throughout the vessel is sufficient to ensure mixing quality. However, since this is a low energy yield process, power consumption becomes a major concern. Power consumption is often easy to measure (torque on the impeller shaft), but can be difficult to predict. This is further complicated by the enormous scale of the vessel, as well as by the rheological difficulties associated with a high solids biomass slurry.

2.6 Scale-up metrics

Scale up of mixing processes can be complicated, as there is no one-size-fits-all approach. Oldshue (1983) in his highly respected textbook, suggests constant impeller tip speed or constant power per unit volume to be a good general rule. This rule assumes maintaining geometric similarity as much as possible. The reasoning is that if the geometric arrangement has proven sufficient for mixing at small scale, the two parameters changing with scale are the total turbulent intensity, which is related to tip speed, or the total energy consumed, which is related to the power per unit volume. This

heuristic is widely applicable to most industrial processes, but is less useful in multiphase

systems, especially high solids applications.

Shao et al (2010) proposed maintaining just suspended speed as a scale up metric

in enzymatic hydrolysis for bioethanol production. This study used wastepaper sludge as

its feedstock. They studied the relationship between reaction progress to mixing

parameters in a laboratory scale vessel, then used CFD to scale up to 750,000 gal. Their

data showed that agitation below just suspended speed proved rate limiting, while

agitation in excess of that did not impact the reaction rate. At scale, just suspended speed

proved to have higher power draw than constant tip speed, but significantly less so than

constant power per unit volume. The biggest limitation to this study was their chosen

solids loading – 1% w/w. While this is reasonable for many liquid-solid systems, it is far

below the standard for bioethanol processes. Furthermore, this low solids concentration

will have significantly different flow properties than a higher solids system. Just

suspended speed is often not a relevant parameter in high solids systems, as the solids do

not settle out at an appreciable rate. At low solids loading, the flow is often Newtonian,

but at high solids non-Newtonian flow begins to occur.

2.7 Rheology of biomass slurries

Dasari et al (2009) studied mixing of pretreated corn stover slurries in the range of

10-25% solids. Data was collected both in a viscometer cup and in a scraped surface

bioreactor. At the beginning of the hydrolysis reaction, the slurries ranged from shear

thickening (10%) to shear thinning (25%). The data were fit to the Oswald power law

model:

$$\eta = Kv^{1-n} \tag{8}$$

where k is a proportionality constant similar to Newtonian viscosity, η is the apparent viscosity, v is the shear rate and n is power law constant. A positive n indicates shear thickening behavior, while a negative n represents shear thinning. An n=0 corresponds to a Newtonian response to shear. At the concentrations tested, the overall apparent viscosity was very high. The presence of high solids concentrations will significantly increase the fluid apparent viscosity, as well as cause non-Newtonian behavior.

Stickel et al (2009) rigorously studied the rheology of corn stover slurries. This work modeled PCS rheology using the Herschel-Bulkley model:

$$\tau = \tau_y + kv^n \tag{9}$$

where τ is the shear stress and τ_y is the yield stress. In this model, n less than 1 indicates shear thinning, while n greater than 1 indicates shear thickening. The yield stress is the minimum amount of stress required before the material will begin to flow. The tested concentration was 15-30% insoluble solids. They reported yield stresses in the range 10-80 Pa for the low end of the range, though increasing concentration by 5% produced orders of magnitude increase in the yield stress. This study also consistently reported shear thinning behavior, which again increased in severity with solids loading.

Pimenova & Hanley (2004) also modeled the rheology of biomass slurries with the Herschel-Bulkley model. Like Stickel, Pimenova reported a strong dependence on solids loading, with higher solids generating more significant non-Newtonian effects. Across the range of 5-30% solids, they reported n values in the range of 0.91-0.05, respectively. The reported yield stress was lower than that reported elsewhere, with a yield stress for a 10% slurry at 2.42 Pa, though the values still changed an order of magnitude with a 5% change in solids loading.

2.8 Mixing in non-Newtonian systems

Mixing in non-Newtonian systems presents a unique design challenge. Wilkens et al (2003) notes that the viscosity changes throughout the vessel, as it is a function of shear rate. Thus, for a shear thinning mixture, the viscosity will be lowest at the tip of the impeller blades, while it will be much higher away from the impeller. As higher solids loading generates stronger non-Newtonian behavior, the solids loading will have a significant impact on the process design. Furthermore, design for these processes is often heavily dependent on the system. Wu & Chen (2008) modeled manure as a non-Newtonian fluid. This study found that the flow patterns were significantly different in the vessel between Newtonian rheology and pseudoplastic (shear thinning) rheology. Shear dependence of rheology impacts how shear propagates away from the impeller throughout the vessel.

Designing mixers in non-Newtonian systems is usually done with approximations. Most famously, Metzner & Otto (1957) defined an effective shear rate for shear thinning fluids, based on the impeller speed N:

$$\dot{\gamma}_{eff} = K_s N \tag{10}$$

where K_s is an empirical constant. They then suggested using this effective shear rate for determining a global apparent viscosity, which could then be used for estimating Reynolds numbers. This work was experimentally validated using helical impellers. Their experimental work was not done on a fluid with a significant yield stress, however, and so applicability has some limitation to it.

Hirata et al (1996) studied the impact of yield stress on the flow field. They found that yield stress tends to promote caverning around the impeller, if the needed

shear amount is not applied. The yield stress prevents shear from propagating away from the impeller like it would in a Newtonian system. Even with high shear rates, dead zones, or unyielded regions of the fluid, often appear in corners of the tank for yield stress fluids. Additionally, the presence of baffles, a requirement for efficient mixing in most applications, can lead to higher power requirement in fluids with very high yield stresses.

2.9 Turbulence in non-Newtonian systems

Turbulence, the primary means by which mixing occurs on a micro-scale, is a poorly understood concept in non-Newtonian systems, relative to Newtonian systems. This exacerbates the difficulty and power associated with scaling up mixing processes, as traditionally turbulence increases with scale. For many non-Newtonian processes, fully turbulent conditions may never be achieved through increased agitation speed (Ghotli et al, 2013). Consequently, at large scale these processes will usually be in the transition regime. Transitional flows can be difficult to predict or model even in Newtonian rheology (Tatterson et al, 1994). Some research has been published on the transition regime for non-Newtonian rheology, though it is largely focused on pipeline flow, rather than mixing tanks.

Desouky & Al-Awad (1998) studied the transition regime in yield-pseudoplastic fluids (shear thinning Herschel-Bulkley fluids). They derived a criterion for predicting the transition based on the ratio of the laminar shear stress to the viscous shear stress. When this ratio is less than or equal to unity, the system was laminar, but in the turbulent region the ratio was greater than unity. Using this they were able to determine the critical Reynolds number and validate it against experiment. This study focused entirely on

pipeline flow, which is a much simpler flow pattern than in stirred tanks. In pipelines the transition regime is much narrower in terms of Reynolds number than in stirred tanks, which means the laminar-to-turbulent transition is much easier to predict and observe.

Malin (1998) also studied Herschel-Bulkley fluids in pipes. His work focused on determining the friction factor under laminar and turbulent conditions. He concluded that the friction factor is not a function of Hedstrom number, and therefore not a function of yield stress, under turbulent conditions. This would be a useful criterion for analyzing the presence of turbulence in pipelines, but the applicability to stirred tanks is necessarily limited.

Bartosik (2010) studied frictional losses in a pipe for kaolin slurry flows. These multiphase flows exhibit significant non-Newtonian behavior and were modelled using both the Bingham model and the Herschel-Bulkley models. By using a modified form of the k-e turbulence model that accounts for the rheological specifics, the author was able to better predict the pressure drop through the pipe section. The author founded that the modified turbulence model predicts behavior well in conditions with low and moderate yield stresses, while the predictions are less accurate for conditions with high yield stresses, indicating that the severity of the non-Newtonian behavior impacts the onset and distribution of turbulence, increasing modelling difficulty.

2.10 Power number

Since total power requirements are dependent on geometry and rheology, often the dimensionless Power number (N_P) is used. Power number is defined as:

$$P_0 = \frac{P}{\rho N^3 D^5} \tag{11}$$

where D is impeller diameter, N is impeller speed, P is total power and ρ is density. Using this dimensionless number, impeller performance can be easily compared in terms of power draw between dissimilar systems. Power number for Newtonian systems is considered inversely proportional to Reynolds number under laminar conditions and constant under fully turbulent conditions (Hemrajana & Tatterson, 2004). In the transition regime, the relationship between Re and N_P is more system dependent. For non-Newtonian flows, the relationship is even more complicated.

Nienow & Elson (1988) studied the relationship between rheology and power number for a wide array of non-Newtonian systems. For shear-thinning fluids, they concluded that impeller power number will be lower in the transition regime than the corresponding value for Newtonian systems. However, a comprehensive survey of their data indicates that sometimes the reverse is true as well – power number is higher for the non-Newtonian system than for the corresponding Newtonian system in the transition regime.

Nouri & Hockey (1998) studied mixing in a shear thinning system. Their results indicated that different impellers can be affected in different ways in transitional, non-Newtonian systems. For a radial flow turbine such as a flat-blade or Rushton turbine, power number was seen to gradually increase in the high transition regime and into the turbulent regime. Conversely, for a pitched-blade turbine, their data showed significant discontinuities between power number and Reynolds number in the transition regime. Clearly, the rheology can create unusual effects on the power number, and therefore total power consumption

Since power number is a dimensionless number, it is assumed that vessel scale

will not affect power number. While the data supports this assumption for Newtonian

systems, there has been no research performed on the effect of large changes in length

scale in non-Newtonian systems. To the author's knowledge, the data herein is the only

published data on the subject.

2.11 Computational Fluid Dynamics

Computational fluid dynamics (CFD) is a numerical technique for solving

complex problems related to fluid flows, heat transfer and transport phenomena in

general. Solving the governing equations for these problems analytically becomes

impossible for anything but the simplest systems. CFD technology originated in the

1950's as computers became an important tool in science and engineering.   As

computers have become ubiquitous and powerful, CFD has become essential, with

applications found in industries such as aerospace, automotives, heat transfer, electronics,

materials processing, HVAC, and many more (Ansys, 2009; Tu et al, 2008).

Many CFD solvers work by discretizing the system spatially into control volumes

called cells, and temporally by time steps. The conditions within each cell are considered

uniform, with cell boundary conditions determined by data from adjacent cells. The

governing equations are solved iteratively via the finite difference method (Chung, 2002).

In this way, the complex process is broken down into thousands of simple problems

which can be solved simultaneously. Common commercial CFD packages include Ansys

Fluent and STAR-CCM+.

The governing equations for CFD problems depend on the particulars of

individual models. All models, at a minimum, must solve the basic conservation

equations for mass and momentum (Ansys, 2009). For the conservation of mass, the continuity equation is solved:

$$\frac{\partial \rho}{\partial t} + \nabla(\rho \boldsymbol{u}) = S \tag{12}$$

Momentum is conserved with the Navier-Stokes equation:

$$\rho \left(\frac{\partial \boldsymbol{u}}{\partial t} + \boldsymbol{u} \cdot \nabla \mathbf{u} \right) = -\nabla p + \nabla \cdot \tau + \boldsymbol{f}_g \tag{13}$$

The shear stress tensor is calculated:

$$\bar{\bar{\tau}} = \mu \left[(\nabla \boldsymbol{u} + \nabla \boldsymbol{u}^T) - \frac{2}{3} \nabla \cdot \boldsymbol{u} I \right] \tag{14}$$

where I is the unit tensor. Other equations can be added for additional complexities in the mode as needed, such as heat transfer, turbulence or chemical reactions. Equations are solved simultaneously in an iterative fashion, so increasing the number of equations used will increase the necessary computational cost. The partial differential equations are reduced to linear, algebraic equations, generally using a Taylor series expansion.

Each iteration, several steps occur to advance the overall solution towards convergence (Ansys, 2009). Firstly, the velocity field is updated based on initial pressure values and solutions to the momentum balance. Next, the continuity equation is solved by making corrections to the pressure based on changes made to the velocity field in the previous step. Thirdly, solutions to any additional models are solved based on the updated solutions to momentum and mass balances. Once all of these quantities are calculated, the stored fluid properties are updated based on the new values. Once these are updated, the solver will check for convergence by evaluating how much these fluid properties changed from the previous iteration to the current. If the change is sufficiently small, then the solution is deemed converged. If not, the updated fluid properties are passed along to the next iteration as initial values, and the process is repeated.

2.11 Discretization for CFD

CFD solutions work on the premise of a discrete domain. While analytical solutions can provide continuous solutions which match the (nearly) continuous nature of real world problems, computational solutions define the domain with a finite number of grid points, at which a solution can be obtained. If each point on a grid interacts with the adjacent points in a predictable fashion, a robust solution can be obtained. If the resolution of the grid is high enough, the discrete nature of the solution can be irrelevant.

The simplest approach to discretizing fluid dynamics equations is the finite difference method. For a sample governing equation (Bhaskaran & Collins, 2002):

$$\frac{du}{dx} + u = 0 \tag{15}$$

The solution domain can be discretized to a finite number of points at locations designated x_i. The governing equation at x_i then becomes:

$$\left(\frac{du}{dx}\right)_i + u_i = 0 \tag{16}$$

Using the Taylor series, this governing equation can be converted to an algebraic equation for its value at any point i:

$$\left(\frac{du}{dx}\right)_i = \frac{u_i - u_{i-1}}{\Delta x} + O(\Delta x^2) \tag{17}$$

If the higher order terms are neglected, then the equation becomes a straightforward, linear, algebraic equation:

$$\frac{u_i - u_{i-1}}{\Delta x} + u_i = 0 \tag{18}$$

A common extension of this finite difference approximation is the finite volume method. The finite volume method defines the computational grid with a series of control volumes, with the center of each control volume called a cell. The finite volume

approach begins with integral forms of the governing equations, rather than differential

forms. For the mass balance equation:

$$\int_s \vec{V} \cdot \hat{n} \, ds = 0 \qquad (19)$$

where $\hat{n}$ is vector normal to the surface of the cell and s is the surface of the cell. This

equation can be discretized by summing up the components from each surface of the

control volume. For the case of a square cell of length Δx and height Δy, if the

components of velocity in the x and y direction are u and v, respectively, the discretized

equation becomes:

$$-u_1 \Delta y - v_2 \Delta x + u_3 \Delta y + v_4 \Delta x = 0 \qquad (20)$$

Using a similar process the other governing equations can be discretized and easily

solved for each cell.

2.12 Multiphase in CFD

Mathematical approaches to multiphase flows can be broadly described in two

categories. The Euler-Lagrangian method treats the secondary phase as discrete

particles/bubbles/drops, and accordingly tracks the motion of each individual particle

(Gerber et al, 2009). This approach is necessary for problems in which the precise

trajectory of individual particles is required. However, the computational expense

increases with an increasing number of particles, as equations must be solved for every

individual particle. Thus there is a concentration limit above which the Euler-Lagrangian

method is no longer feasible. Conversely, the Euler-Euler method treats both primary

and secondary as continuous phases. The Euler-Euler method comes in several forms:

the volume of fluid model, the mixture model, and the general Eulerian model.

The volume of fluid model treats all phases as continuous phases. The key use for this method is tracking a surface or boundary between phases. The flow of each phase is treated independently, and there is an additional volume fraction term. The volume fraction is assumed to be 0 or 1 throughout most of the system, as the phases do not readily interpenetrate. At the boundary of the regions, the volume fraction will be some value between 0 and 1. The fraction assumes that within the cell, some portion of the secondary phase is present in the specified fraction, but the boundary between the phases is a well defined surface. There is not a significant gradient. This method is well designed for modeling relatively immiscible fluids, such as oil-water flows or air-water flows. The mixture model assumes greater interaction between the primary and secondary phases. In this method, a modified momentum equation is solved to govern both phases. This method works well in systems in which the phases are primarily driven in the same flow pattern. The third method is the most robust of the Euler-Euler techniques. The true Eulerian method solves all of the governing equations for each phase. The pressure for each phase is coupled together, thus linking the solutions for each phase. This method will not distinguish individual particles, but rather assumes that any discrete unit of the secondary phase is much smaller than the surrounding cell (Ansys, 2009). The volume fraction for each phase in this method is calculated from a form of the continuity equation:

$$\frac{\partial}{\partial t}\left(\alpha_i \rho_i\right) + \nabla \cdot \left(\alpha_i \rho_i \mathbf{u_i}\right) = \sum_{j=1}^{n}(m_{ji} - m_{ij}) \tag{21}$$

where α is the phase volume fraction, i and j designate phases, and m is the mass exchange between the indicated phases.

2.13 Passive scalars in CFD

Passive scalars are quantities which are affected and transported by the fluid flow, but do not themselves affect the flow. They can provide essential data regarding the motion of the fluid. They are governed by the passive scalar transport equation (Ansys, 2009):

$$\frac{\partial \rho \phi_k}{\partial t} + \frac{\partial}{\partial x_i}\left(\rho u_i \phi_k - D_k \frac{\partial \phi_k}{\partial x_i}\right) = S_{\phi_k} \tag{22}$$

where D is the diffusivity coefficient and S is a user defined source term. This equation has the form of the advective-diffusive equation. In a multiphase system, if the scalar is confined to a single phase, every instance of ϕ_k is replaced with $\alpha \phi_k$, where α is the phase volume fraction. If the scalar is spread throughout the mixture, phase averaged terms are used.

CHAPTER 3. EXPERIMENTAL

3.1 Work plan

First, multiphase mean age theory (MMA) was derived. The derivation was
validated by comparing MMA distributions with residence time distributions determined
both computationally and experimentally. Following a favorable comparison, MMA was
applied towards measuring just suspended speed (N_{jss}) in stirred tank vessels. Novel zone
definitions allowed for measuring N_{jss} across a range of particle densities, particle sizes,
and solids concentrations. Lastly, higher solids slurries were investigated for effect of
scale and rheology on power requirements. A laboratory scale model for non-Newtonian
slurries was validated against experimental results and then scaled up to million gallon
scale. Multiple impeller designs, sizes, and locations were investigated to determine the
effect on the power number and the flow patterns through the vessel.

For developing a multiphase mean age technique for analyzing mixing quality, a
CFD model was built. The geometry was a 100m section of pipe, 24in in diameter. Data
was collected 80m and 100m downstream. The fluid was a 95-3-2% mixture of water, oil
and air, respectively. Since the section was to be in the middle of a 37km pipeline, the
simulation was run to obtain outlet boundary, then the outlet conditions were set to be the
inlet conditions, and then the simulation was run again. This procedure was repeated
until the inlet and outlet conditions showed no significant difference, indicating a steady
state profile. Once a steady state flow field was obtained, three passive scalars were

included with a value of zero at the inlet as well as a source term. One scalar was

confined to the oil phase, the second was confined to the water phase, and the third was

calculated for the entire mixture. The resulting scalar solutions were the mean age

solutions. The mean age solutions were compared against an unsteady state residence

time solution. This solution incorporated two scalars (one for water, one for oil) with a

finite value at the inlet at time zero, indicating a pulse input. The concentration of the

scalar at the outlet was tracked, and the simulation run until all the material passed

through the section of pipeline. The resulting unsteady residence time distribution was

compared against the steady state mean age distribution, and both distributions were

compared against experimental data from Sugiharto et al (2009).

In order to apply multiphase mean age to predicting just suspended speed, several

CFD models were created. The first was a two dimensional mixing vessel with inlet and

outlet, as well as a narrow zone along the bottom of the vessel. The system contained a

95-5% water-sand mixture. The inlet flow rate was set to be arbitrarily low, and the

impeller speed was varied across a wide range. In each run, a passive scalar, confined to

the sand phase, with a source term and a zero value at the inlet was used to develop a

mean age profile. The average mean age in the bottom zone was calculated and recorded

for each impeller speed. The simulations were repeated with the scalar only calculated

within the bottom region, with the scalar value defined as zero elsewhere in the vessel.

The series was run a third time, this time with the inlet and outlet boundaries changed to

walls, and again the scalar was only calculated in the bottom region. These data series

were compared to prove the viability of the closed system technique for analyzing age

only in small sections of a larger system. Following this, the closed system technique

was applied in a three dimensional system. Solid concentration was compared across a range of 0.5-12% (w/w) with Rao et al (1988). The particle size was varied across a range of 75-200 microns and the solid density across a range of 1400-2500 kg m^{-3} with Armenante et al (1998).

The effect of scale and rheology on high solids biomass slurries was studied through both experimentation and simulation. Firstly, the slurry was characterized. A 12.5% insoluble solids concentration was chosen to represent a high concentration slurry. Above this value, the material starts to behave like a solid, while below this value the material behaves as a low concentration mixture. The rheology of this slurry was characterized using a downward shear sweep in a cup-in-vane rheometer. The data were fit using the Herschel-Bulkley model. Then, a 2kg batch was mixed in a 2L vessel with a hemisphere bottom, using a pitched blade turbine. The material was mixed across a range of impeller speeds of 100-1000 rpm, and the average torque was recorded. Additionally, the cavern size was measured at 900 rpm. Then a CFD model was built. The same geometry was used as the laboratory scale mixing tank. The viscosity was specified using the parameters measured in lab. The model was run across a range of 100-1000 rpm, and matched to the experimental data for torque and cavern size.

Following validation, the CFD model was scaled up to million gallon size. Two of the shelf impellers were tested – namely, a pitched blade turbine and an A310 hydrofoil. Each impeller was tested across a range of impeller speeds of 25-65 rpm, two different impeller clearances (CT^{-1} = 1/3, 1/2) and two impeller diameters (DT^{-1} = 1/3, 1/2). Three different turbulence models were employed – laminar, RNG k-e, and k-w SST. In each case, total power and power number were calculated. The vector flow field

was examined qualitatively, and the apparent viscosity contours were analyzed qualitatively.

3.2 Equipment

All CFD mesh generation was performed with Ansys Icem vs 12, 13 and 14. CFD simulations were conducted using Ansys Fluent vs. 12, 13 and 14. No discernable impact on the results was detected between these versions. All simulations were conducted on a custom designed supercluster at the University of Louisville.

The slurry viscosities were measured using a Physica MCR 300 Modular Compact Rheometer from Anton Paar (Ashland, VA). Slurries were homogenized in a laboratory-scale Resodyn Acoustic Mixer (LabRAM). Validation of the high solids CFD model was performed in a 2-L batch vessel. The vessel diameter was 14 cm, and the bottom was hemispherical. The impeller was a 45 degree pitched blade turbine (PBT) with a diameter of 6.5 cm ($DT^{-1} = 0.5$). The impeller clearance was 7 cm ($CT^{-1} = 0.5$). The torque required to turn the shaft was measured at steady state with a torque meter from Sensor Developments, Inc.

3.3 Materials

The corn stover, pretreated with dilute sulfuric acid at 190 C, 1.6 % acid, 30 % solids, and 5 min residence time, was supplied by the NREL. An insoluble solids (ISS) concentration of 12.5 % was used as a representative middle ground rheology for studying mixing. Actual operation would likely range from a starting point a few percent solids higher to a few percent lower, as cellulose becomes hydrolyzed.

3.4 Procedures

3.4.1 Rheology measurements

To determine rheological parameters, first a slurry must be prepared. Samples of pretreated corn stover (PCS) were first weighed, then vacuum filtered and then dried in an oven overnight at 105 degrees C to determine moisture content. Following this, fresh PCS was used to make a 50g slurry. PCS first, then water, were added to obtain 50g at the desired solids concentration. This slurry should be completely mixed with the LabRAM mixer for 60 s, then transferred to the rheometer cup (Figure 3.1). Ensure that the fill level in the cup exceeds the fill line midway up the side of the cup.

Figure 3.1: Rheometer cup

Prepare the rheometer for measurements by turning on the power supply with the switch on the back (Figure 3.2). Turn on the circulation pump with the switch on the

Figure 3.2: View of rheometer, circulation pump and power supply

front. Turn on the rheometer itself with the switch on the back. Turn on the air supply at

the regulator valve (Figure 3.3). Lastly, turn on the connected PC and load the Rheoplus

program.
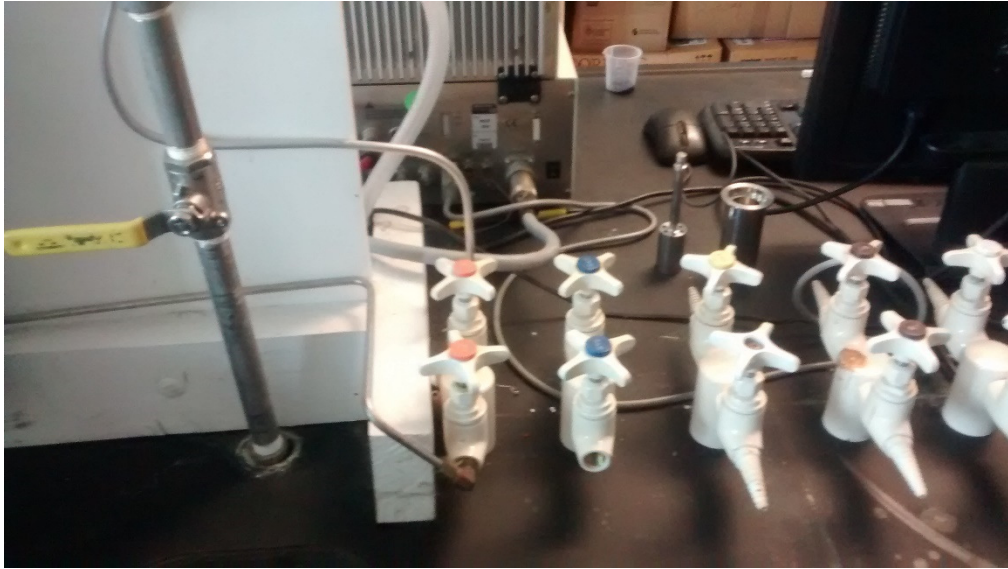
Figure 3.3: View of air supply valve

Inside Rheoplus, select the Setup Rheometer button (Figure 3.4). In the dialog
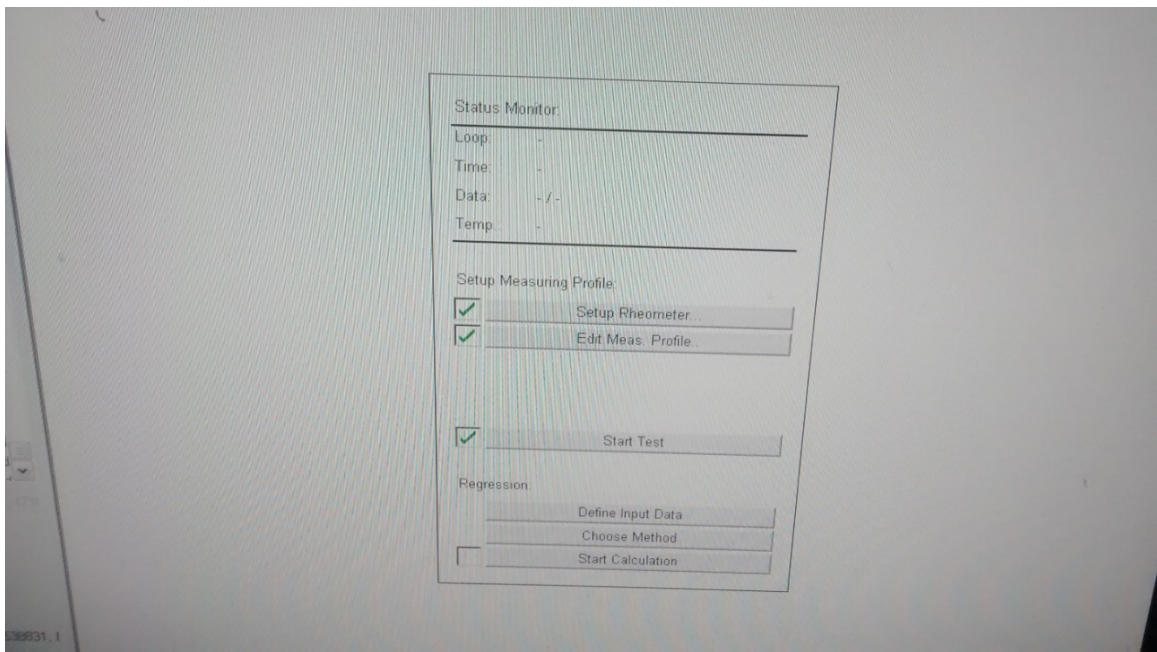
Figure 3.4: Rheoplus menu

box (Figure 3.5), press the Initialize button and wait for the initialize process to complete.
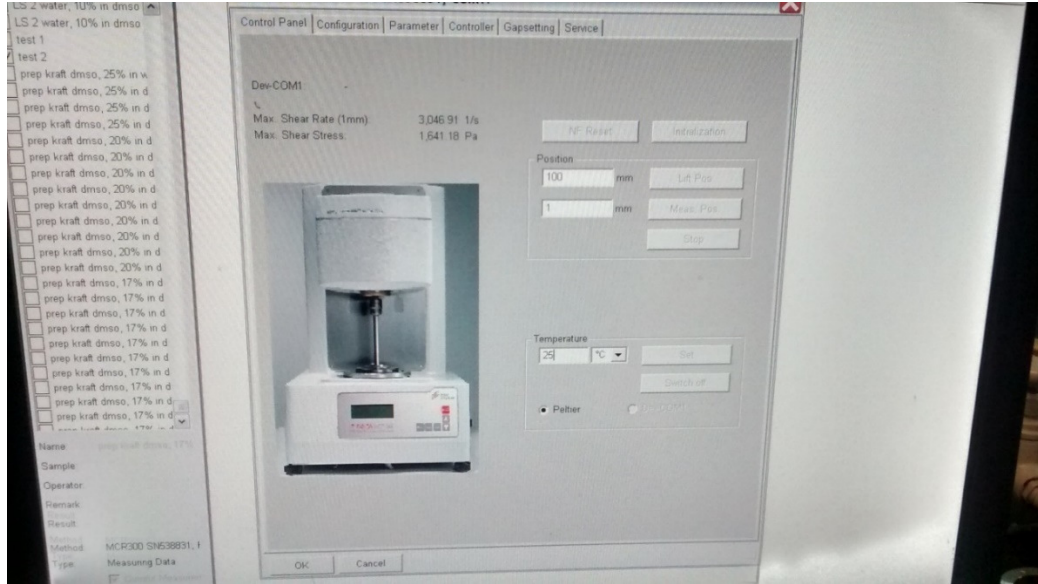
Figure 3.5: Setup rheometer menu

Once initialization is complete, specify the process temperature (25C). Install the

measurement cup into its slot. Install the vane impeller into its coupling. Then press

Measurement position to engage the impeller into the cup. Close the Setup Measurement

Device dialog.

Next, select the Edit Measurement Profile button (Figure 3.6). Select the 'Interval
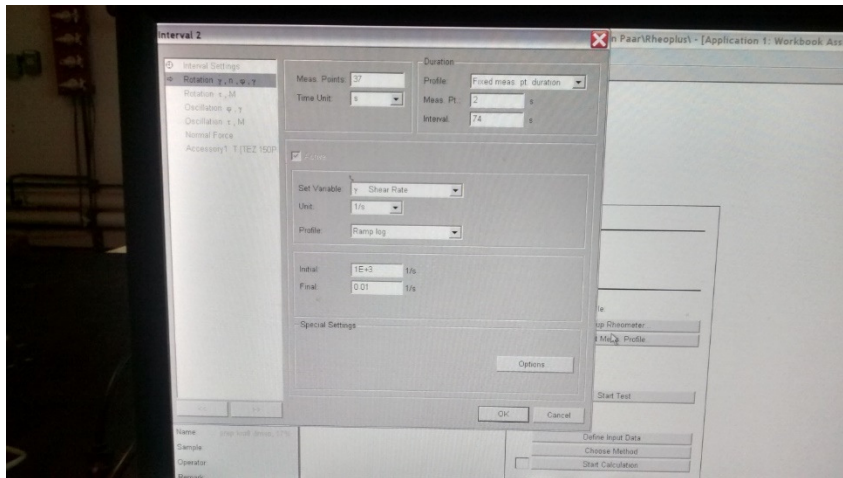
Figure 3.6: Edit measurement profile menu

Settings' tab, and specify '2' for the number of intervals. Next choose the first 'Rotation'

tab. Specify 1 for 'Meas. Points.' Specify 180 for 'Meas. Pt.' in the 'Duration section.

Then choose 'Constant' in the 'Profile' drop down. Specify 170 for the speed. This will

premix the sample according to the procedure reported by Dunaway et al (2010), which

involves estimating the minimum mixing speed using Zwietering's (1958) correlation for

mixing tanks. Next, select the second 'Rotation' tab. Specify the desired range of shear

rates in the dialog (suggested values would be from 1000-50 s^{-1}). Ensure that the higher

value is the initial shear rate and the lower value is the final. Close the Edit Measurement

Profile dialog.

Next, select Start Measurement. Give an appropriate name for the trial, and press

Start Measurement (Figure 3.7). Do not disrupt the rheometer while data collection is
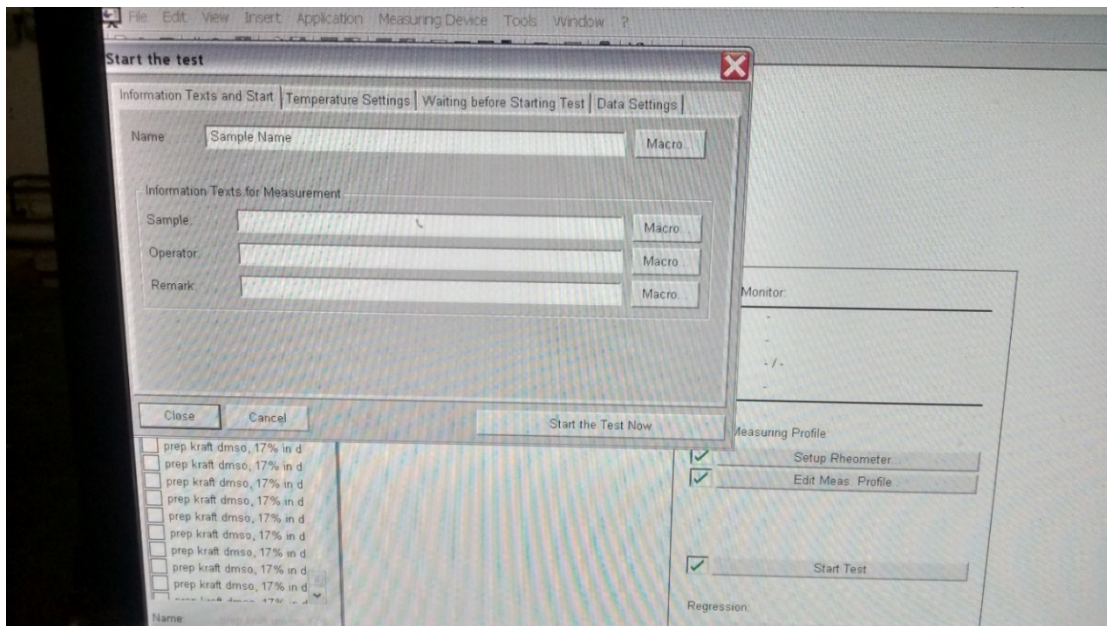
Figure 3.7: Start measurement menu

occurring. After the data has been collected, select View Data Table. These data can be

fitted to the appropriate rheological model using regression. Repeat the trial at least

twice more to ensure consistency of data, and average the results.

Lastly, select Setup Measurement device again. Press Lift Position to raise the viscometer head. Remove the vane and cup, dispose of the material properly, then wash and dry the cup and vane. Repeat these steps for other solids concentrations.

3.4.2 Torque measurements

Using the moisture content measured above, prepare a 2000g sample in a large beaker. Add the necessary solids first, then add the required water to achieve the total sample mass. Using a large stir rod, preliminarily mix the sample to ensure that all the solids are wetted. Transfer the sample into the mixing vessel. Place the impeller in the mixing vessel at the pre-measured height (Figure 3.8). Press the Power button on the

Figure 3.8: Lab-scale vessel. Tape line indicates the target fill level

motor. Set the impeller speed to 1000 rpm and press Start. Allow the slurry to homogenize at this impeller speed for approximately 30 minutes.

Following homogenization, adjust the impeller speed on the motor to the desired setting. Turn on the torque sensor by pressing the button once. Watch the range of fluctuation on the torque sensor for 1-2 minutes. Record the high and low values in oz-in. Adjust the motor speed to any other desired impeller speeds. Upon completion, properly dispose of the sample, and thoroughly wash and dry the impeller and mixing vessel.
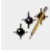
3.4.3 Cavern size measurements

Prepare a sample as described in the previous section (or perform this measurement using the same sample). Transfer the sample to the mixing vessel. Turn the motor on, set the impeller speed to 1000 rpm, and press start. Homogenize the sample for approximately 30 minutes. Following homogenization, adjust the impeller speed on the motor to the desired setting. Wait 5 minutes for the flow field to fully adjust. Look on the side of the vessel to see if motion can be observed. If not, choose a higher impeller speed. If so, measure the distance from the top of the moving section to the top of the slurry. Measure this distance at the midpoint between the baffles. Repeat this measurement for all four sides of the vessel. If motion extends to the surface of the slurry, no caverning is observed, and the experiment should be repeated at a lower impeller speed. Upon completion, properly dispose of the sample, and thoroughly wash and dry the impeller and mixing vessel.

3.4.4 CFD procedures

The first step to creating mesh is building geometry. Points are defined, then the points are connected with lines. The lines are connected together to form surfaces. Closed shapes bounded by surfaces can be filled with bodies. Surfaces and bodies form the architecture upon which mesh is placed. Mesh is generated, then imported into the CFD solver. Materials, phases boundary conditions, etc are specified, then the simulation is run. Once the simulation has converged, the data are analyzed. Directions for building and simulating the industrial scale mixing tank from Ch 6 will be given in detail to demonstrate how the software works, then specifics for Ch 4 and Ch 5 will be given.

3.4.4.1 Meshing

To begin creating a mesh file of a tank with a hydrofoil impeller, open ICEM to a new, blank project. Click the *Create Point* button: on the ribbon bar at the top. Then, in the *Create Point* dialog on the left, select the *Explicit coordinates* button: XYZ. Since the default position for the placement of a point is the origin, this will serve as the starting location (1). Select this point by pressing the *OK* button: . More points will then be created to draw an outline of tank. Once an initial point is created, the *Base Point and Delta* option can be used to more easily create the rest of the point. This allows one to create a new point by locating it in reference to the base point. Use this option to create points at deltas (2)(0,17,0), (3)(8.5,-1.5,0) and (4)(8.5,17,0) (Figure 3.9).

The points are then connected by creating curves. Begin to do so by selecting *Create/Modify Curves* on the ribbon bar. From here, select *From Points* . With this tool, selecting multiple points will cause ICEM to draw a best fit line between the selected points, in the order in which they were selected. If only two points are selected,

Figure 3.9: Initial geometry points in Icem

the line will invariably be straight. Otherwise, it will reflect the geometry of the points.

Use this tool by selecting points with a left click, then ending the curve with a center

click. If an errant point is selected, back up by using a right click. In this manner, create
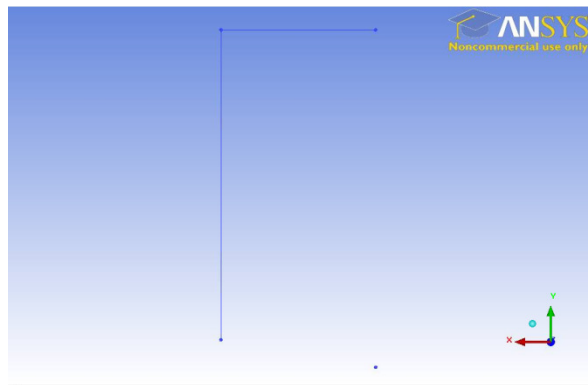
two curves to connect (1)-(2) and (2)-(4) (Figure 3.10).

Figure 3.10: Curve creation in Icem

The two curves just created will be used to create surfaces that form the top and

side wall of the tank. To do so, they must be revolved about an axis to create a surface.

Select *Create/Modify Surface* from the ribbon bar. Next, on the left, select *Surface of*

Revolution . Keep the start angle at 0, and change the end angle to 180. Choose (3)

& (4) for the axis points, and then center click. Then, select the two curves and center

click again. This should form a circular and a cylindrical surface, as well as additional

37

points and curves to define them. By left clicking and dragging on the image, the view can be rotated to get better a perspective of the 3D nature of the model (Figure 3.11).
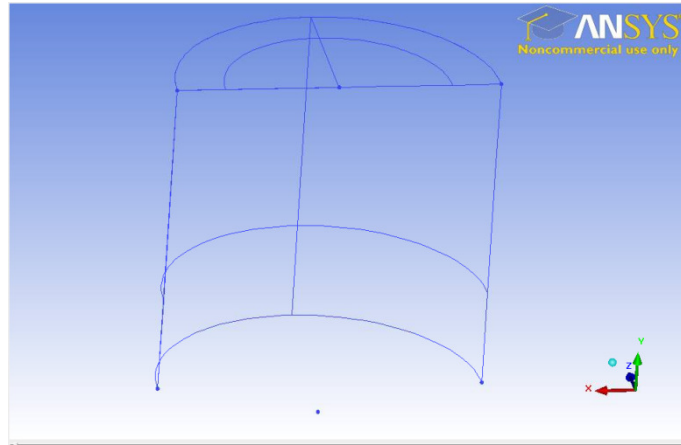

Figure 3.11: Revolved surfaces in Icem

Next form the bottom of the tank. Select *Create/Modify* C*urves* again, and then *From Points.* Create a curve connecting points (1), (3) and the newly created point (5) opposite of (1). This should create a dish shaped arc. The arc now needs to be cut in half. Select *Segment Curve* from the *Create/Modify Curves* menu. The default mode is *Segment by Point*, which is correct. Select the newly created arc for the curves, center click, and then select point (3). Center click, and the curve will be split in two at point (3). To reduce clutter, delete the curve on the right. Choose *Delete Curve* from the ribbon bar, select the curve on the right, and then center click. Use the *Surface of Revolution* option to revolve this new curve around in the same manner as above to form the bottom of the tank (Figure 3.12).

The baffles are formed next. Return to creating points by the *Base Point and Delta* option. Beginning with point (2) as the base, create a point (6) offset by (.4, -.5,.1). Select point (6) as the new base point, then create three new points at deltas: (7)(2,0,0),
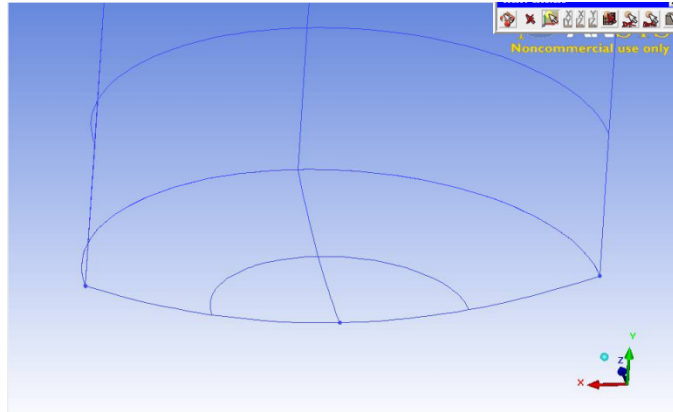
38

Figure 3.12: Bottom surface of vessel

(8)(0,-16,0) and (9)(2,-16,0). On the ribbon bar, select *Transform Geometry* . Then

click *Translate Geometry* on the left. Select points (6)-(9), then center click to keep

the selection. Check the *Copy* check box so that four new points can be created. Ensure

that *Explicit* is selected for the translation method. Then input an offset of (0,0,-.2).

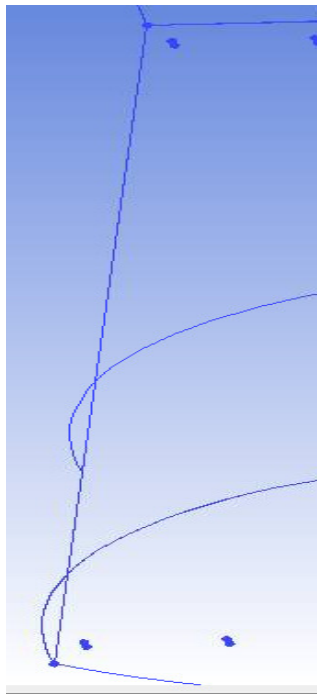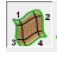Click apply, and new points will be created (Figure 3.13).

Figure 13: Corner points for baffles

Using the *From Points* option for creating curves, connect each of the eight points just created to form an enclosed box. This will require 12 curves. Now enclose the curves with faces. To do this, on the *Create/Modify Surfaces* menu, select *Simple Surface* . The default method is *From 2-4 Curves*. This is correct. Select each of the four curves that form a face to the baffle, and center click. Repeat this process until all six faces have been created (Figure 3.14).
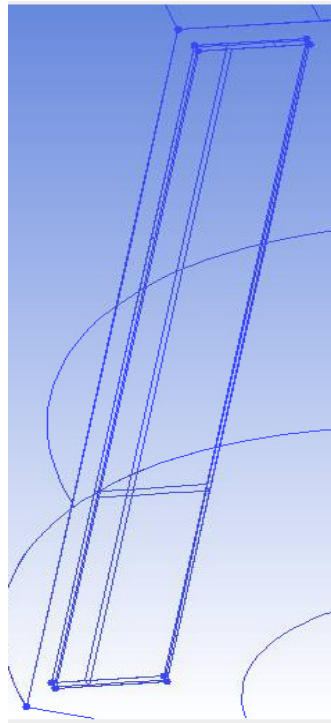

Figure 3.14: Baffle with faces

The created baffle must now be moved into position. Click *Transform Geometry* again, and this time choose the option *Rotate Geometry* . Select the points, curves, and surfaces associated with the baffle. Make sure that *Copy* is unchecked. Check the Angle box, and input -45 degrees. Since the y-axis is vertical, choose it for the rotation axis. For *Center of Rotation*, select *Specified* under *Center Point*. Then, select point (3) for the center point and click *Apply*. This should rotate the baffle into the tank. While

the rotated baffle is still selected, check *Copy*, and then change the angle to -90. Pressing

Apply again will create a second baffle opposite the first in the tank (Figure 3.15).
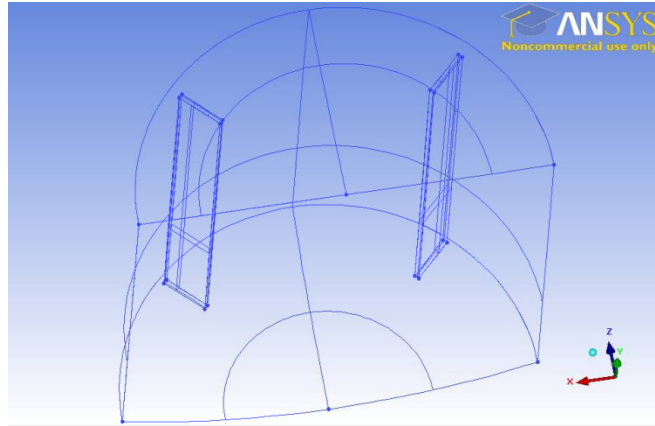

Figure 3.15: Duplicated baffles

The impeller shaft is created next. Starting from point (4) and using the *Base*

Point and Delta option, create a point with the offset (0,-.53,0). Select the new point as

the base point, and create at the offset (-.434,0,0). Repeat for the following deltas, each

time selecting the newly created point as the base point for the next:

(0,-5.53,0)

(-.409,0,0)

(0,-.775,0)

(-.422,0,0)

(0,-1.69,0)

(1.265,0,0)

Connect these eight points with 7 straight-line curves. Do not connect the last point back

to the first point. Using *Surface of Revolution*, revolve the curves about the center 180

degrees, with points (3) & (4) as the axis points. With the *Simple Surface* tool, enclose

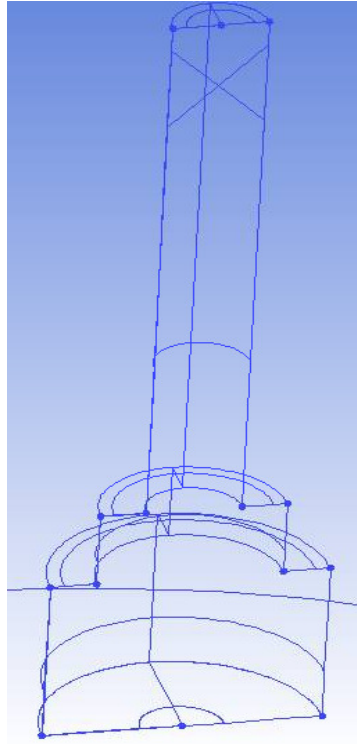the impeller shaft with a surface (Figure 3.16).

Figure 3.16: Impeller shaft with faces

Beginning with the last point created as part of the impeller (the bottom center of the shaft), use the *Base Point and Delta* option to create the following points, each time choosing the new point as the next base point:

(0,-2.133,0)

(-4.722,0,0)

(0,3.820,0)

(2.513,0,0)

(0,6.308,0)

With *From Points*, connect the points using six curves. Begin connecting the bottom of the impeller to the first created point, and end by connecting the last created point to the upper left corner of the impeller shaft. The *Surface of Revolution* tool should be used to revolve these six curves 180 degrees about the same axis as above. This frame will form

the boundary between two separate fluid regions, which comprise the moving reference frames in Fluent. Enclose this region with 2 surfaces using the *Simple Surface* tool. The surfaces should be bounded by the curves just created, as well the curves forming the edges of the impeller shaft (Figure 3.17).
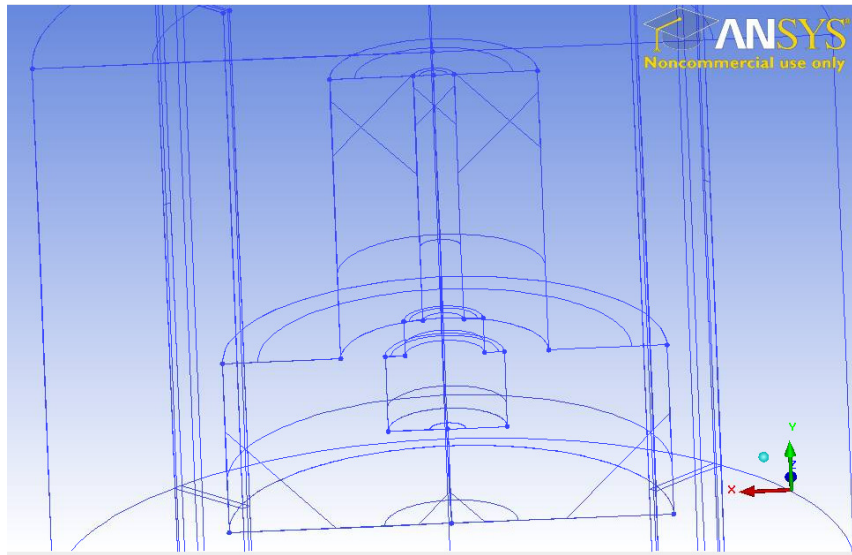

Figure 3.17: Boundary of rotating zone

Next, notice the gap between the impeller shaft and the top and bottom of the tank. This gap was created so that the rotating and stationary walls will not intersect, which can create instability during calculation. However, to properly form the periodic boundary, there should be some connection, Therefore, curves must be created. Using the *From Points* tool, connect point (4) to the top center point of the impeller shaft. Then, connect point (3) to the bottom center of the fluid zone boundary. Once this is done, two surfaces can be created to enclose the outer fluid region. Navigate to the *Simple Surface* tool. Under *Method*, change the option to *From Curves*. The surfaces about to be created are too complicated for the default method. Now, select the three curves defining the left side of the tank, the two curves just created at the tank center, and

the curves defining the left side of the fluid region boundary. This defines one side of the periodic boundary. Repeat using the right side curves (Figure 3.18).
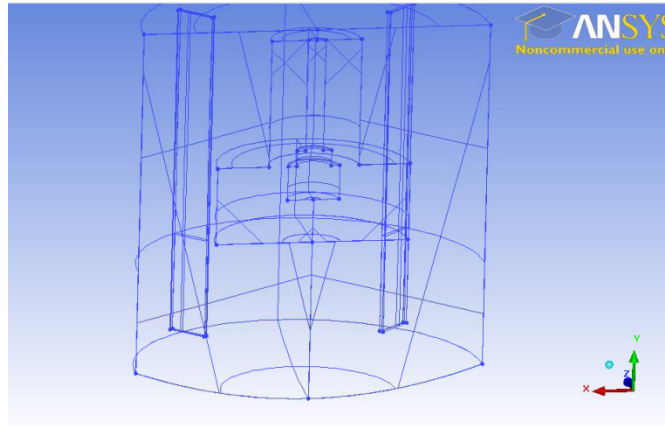

Figure 3.18: Periodic face creation

The last geometry elements to be created are the impeller blades. Due to the curved nature of the blades, combined with the cylindrical shaft to which they are mounted, these are the most complicated objects to create in the model. Open the *Base Point and Delta* tool for creating points. Use the point at the bottom left corner of the impeller shaft as the base point for all of the following deltas (Figure 3.19):

(.2,0,-.453)   (10)

(.2,.112,-.607)   (11)

(.2,.194,.096)   (12)

(.2,.301,-.066)   (13)

(.2,.662,.453)   (14)

(.2,.774,.299)   (15)

(-2.985,.200,-.453)   (16)

(-2.985,.312,-.607)   (17)

(-2.985,.291,.006)   (18)

(-2.985,.391,-.134)   (19)
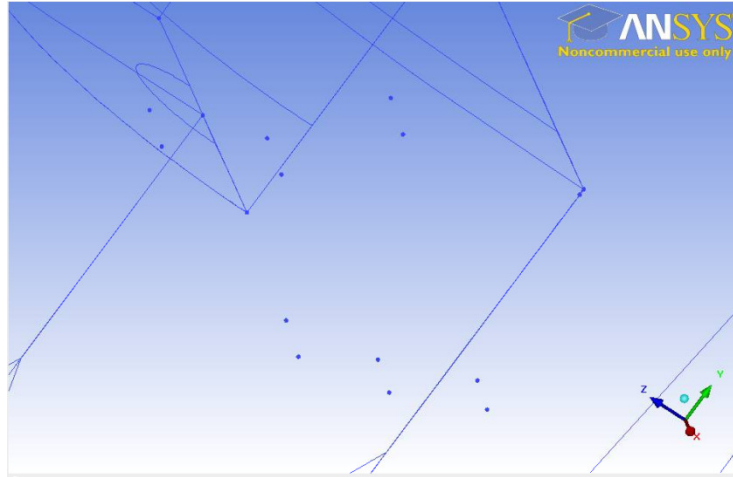
(-2.985,.473,.438)   (20)

(-2.985,.563,.315)   (21)

Figure 3.19: Outline points for impeller blade

Now using *From Points*, create the following curve connections (Figure 3.20):

(10)-(12)-(14)   [a]

(11)-(13)-(15)   [b]

(16)-(18)-(20)   [c]

(17)-(19)-(21)   [d]

(10)-(16)   [e]

(11)-(17)   [f]

(14)-(20)   [g]

(15)-(21)   [h]
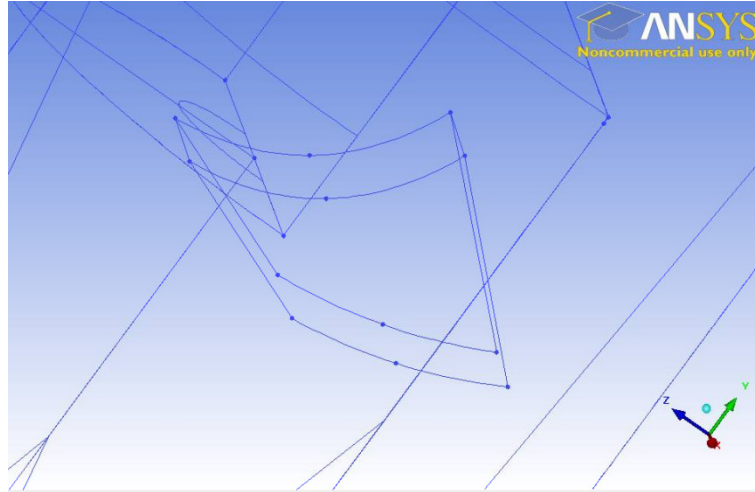
(10)-(11)   [i]

(14)-(15)   [j]

(16)-(17)   [k]

(20)-(21)   [l]

Figure 3.20: Outline curves for impeller blade

Using the *Simple Surface* tool, change the method back to *From 2-4 Curves*. Create

surfaces along the four long faces of the blade (Figure 3.21):

[a]-[e]-[c]-[g]
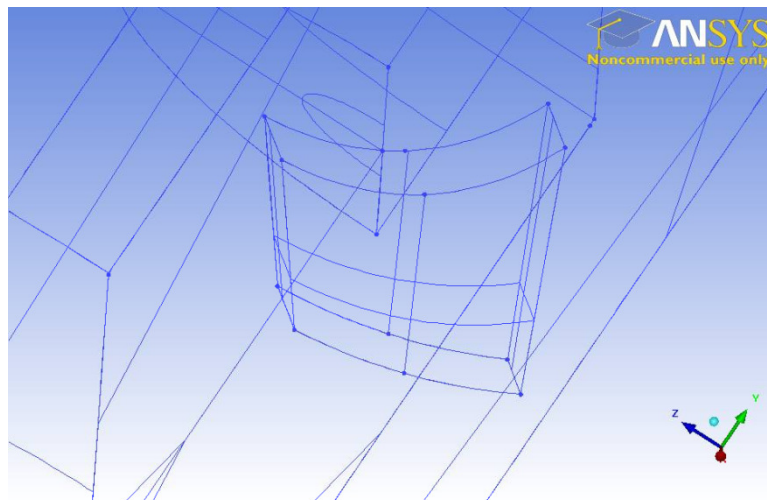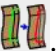
[b]-[f]-[d]-[h]

[i]-[e]-[k]-[f]

[j]-[h]-[l]-[g]

Figure 3.21: Surfaces for impeller blade

Now, using the *Rotate Geometry* tool, rotate the points, curves, and surfaces -30 degrees about the same axis previously used (points (3) & (4)). With the blade rotated into position, it can be properly attached to the impeller shaft. To do so, select *Create/Modify Curves* from the ribbon. On the left, select *Surface-Surface Intersection* [icon]. With this tool, left clicking on two intersecting surfaces, followed by a center click, will create a curve where the two surfaces intersect. Use this tool to create four curves where the four long surfaces intersect the cylindrical surface of the shaft. Next those long surfaces must be trimmed so as to include only the portion that is outside of the impeller shaft. Select

Create/Modify Surfaces from the top, and then choose *Segment/Trim Surface* [icon]. With this tool, left clicking a surface, center clicking, then left clicking an intersecting curve, and finally center clicking will split the surface along the curve. Use this tool to segment the four long faces of the impeller blade along the four newly created intersection curves. Now that the blade faces are self contained outside of the shaft, the geometry inside the

shaft should be removed. Use the *Delete Any Entity* [icon] feature on the ribbon bar to remove the points, curves, and surfaces inside of the impeller shaft originally associated with the blade (Figure 3.22).
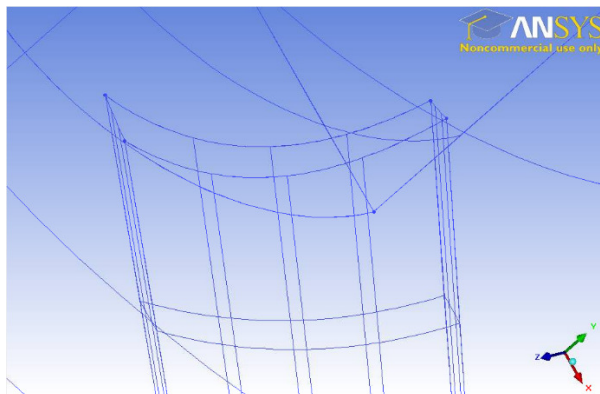

Figure 3.22: Trimmed impeller blade base

Now, enclose the two tips of the blade (one is flush against the shaft) with a surface, again using the *Simple Surface* tool. Using the *Rotate Geometry* tool, ensuring that *Copy* is checked, create two copies of the blade (points, curves and surfaces) at -60 degree angles about the (3)-(4) axis. At this point there should be three impeller blades inside the tank (3.23).
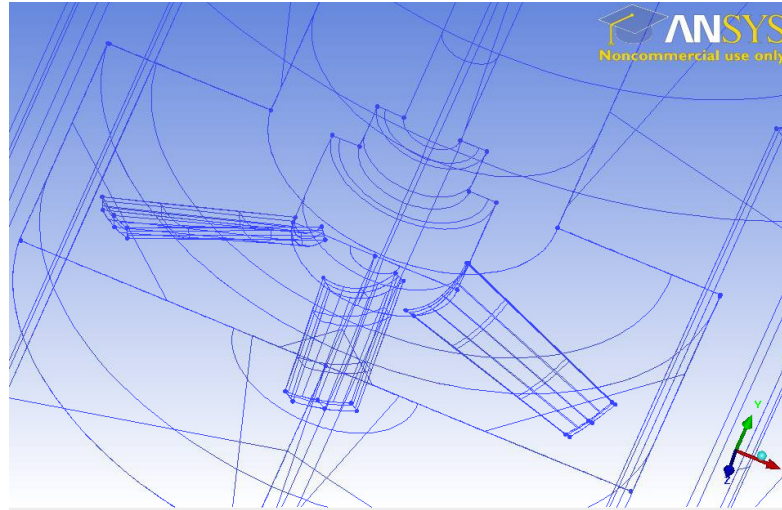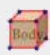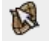

Figure 3.23: Duplicated impeller blades

The geometry is now complete and can be prepared for meshing. Rename features for better sorting. On the side bar above the menus, right click on *Parts*, and select *Create Part* [Create Part] . The part name can be entered in the text box labeled *Part*. Then by selecting *Entities*, specific geometry elements can be assigned to the new part. By default, the geometry is assigned to a part called 'GEOM'. This name will be retained for the tank walls, but new parts should be created for other geometry elements so that they can be easily identified once the mesh is imported into Fluent.   Create a part called 'BAFFLES' that includes all geometry (points, curves, surfaces) associated with the baffles. Create 'IMPELLER' to include both the shaft and the blades. Create 'Blend' to include the interface between the two fluid zones. Finally, create four parts which will

become the periodic boundary conditions in Fluent. Create two parts ('INT' and 'INT2') to contain the two faces connecting the impeller edge to the edge of BLEND. Then create two parts ('EXT' and 'EXT2') which contain the faces which connect the edge of BLEND to the tank wall. Labeling each of these four faces separately makes it easier to set the proper boundary conditions later.

The next step is to create bodies, which contain 3D mesh and are bound by the curves and surfaces previously created. On the ribbon bar, select *Create Body* . On the left, text can be entered into the drop box labeled *Part*, so that each body can have its own part associated with it. Choose the option *By Topology* , and then the method *Selected Surfaces*. The *Select Surface(s)* button allows the user to select the surfaces which create a bounded, closed region which will form the new body. Use this to select the six faces of one of the baffles, naming the body 'BAFFLE1.' A center click will create the body, noted by a label on the screen. Similarly, create the following bodies:

BAFFLE2

BLADE1

BLADE2

BLADE3

SHAFT

These are all the solid zones, which have simpler geometry than the two fluid zones. The interior fluid zone body 'INNER' should be bounded by BLEND, INT, INT2, and the surfaces of IMPELLER which face the interior of the tank. The last body 'OUTER' should be bounded by BLEND, EXT, EXT2, and GEOM. Since the baffles are self contained within the body, it is not necessary to include them in the body definition. At

some point in creating these bodies, ICEM might prompt to run *Build Topology*. If

prompted, allow it to do so. This is simply a feature that corrects truncation errors in the

placement of the geometry. It might create new points or segment curves, but it will not

change the shape or geometry (Figure 3.24).
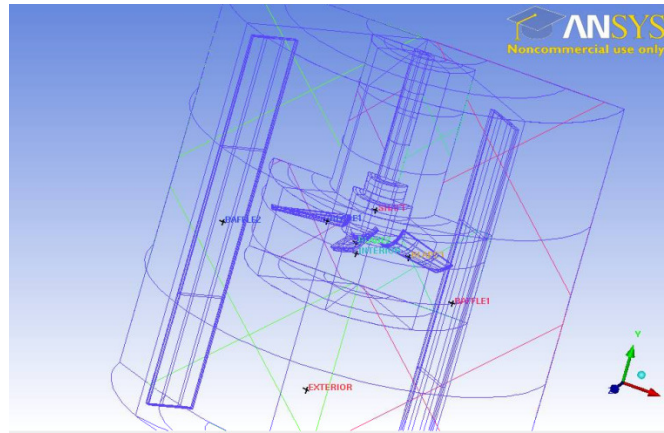
Figure 3.24: Final geometry model

The last thing step before the geometry is meshed is to specify the mesh density.

A denser mesh is necessary around intricate details. On the ribbon bar, select the *Mesh*

tab [Mesh].   Then choose the button for *Surface Mesh Setup* . Use the *Select*

Surface(s) button to choose surfaces, and then specify the *Maximum Size*. Use this tool

for specifying maximum sizes on the following surfaces:

Large Baffle faces	2
Top of tank	2
Side of tank	2
Bottom of tank	2
Ext	1.25
Ext2	1.25
Int	1.25

Int2   1.25

Bottom of Blend   1.75

Wider cylinder of Blend   1.75

Top of wider cylinder   1.75

Narrower cylinder   1.5

Top of Blend   1.5

Large faces of Impeller blades   0.35

Next use the *Curve Mesh Setup* 🪝 tool on the ribbon bar. Select curves using the *Select Curve(s)* 🖎 button, then specify the *Number of nodes* for the following curves:

Long edge of baffles   64

Bottom round edge of shaft (from left to right)   19, 27, 27, 8

Top edge of bottom shaft section   76

Top and bottom of second section   57

Bottom of third shaft section   38

Top of shaft   95

Verticals of top shaft section   43

Then, select *Global Mesh Setup* 🖼 from the ribbon. On the left, choose *Global Mesh Size* 🖼. Then, for the scale factor, choose 0.4. The Global Mesh Size can be adjusted to easy change the overall mesh count, without altering the distribution of the cells (such as during a sensitivity analysis). ICEM is now ready to generate the mesh. Press the *Compute Mesh* button 🌐 on the ribbon, then press 'Compute' on the left. The

default settings are sufficient. ICEM will take a few minutes to generate the mesh (Figure 3.25).
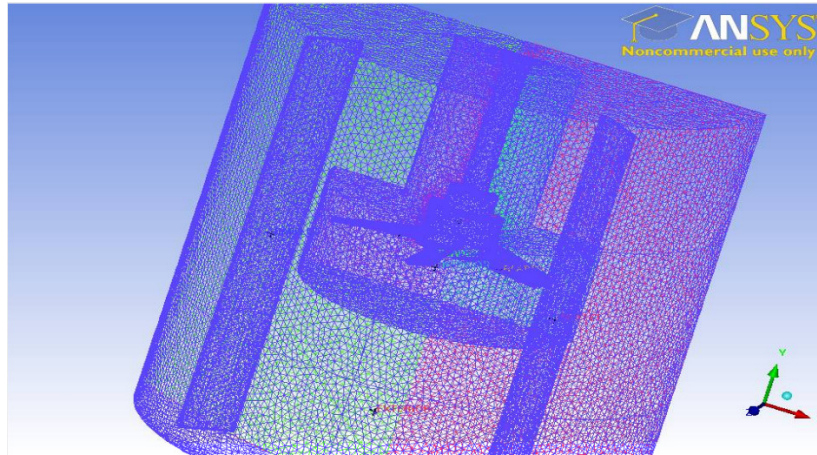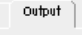
Figure 3.25: Meshed geometry

When it is done, choose the *Output* tab [Output] from the ribbon bar, and then press *Export to Fluent V6* ✳ on the ribbon. When prompted about 'Family Boundary Conditions' press 'Accept.' When prompted about saving the project, do so. Then ICEM will prompt to open a file. Ensure that the *.uns file that matches the name of the current project is chosen, then press 'Open.' A popup menu will appear, asking to specify the output file. Choose a name and location which can be easily found, then press done. The mesh will be output in a .msh file, which can be imported into Fluent (Figure 3.26).
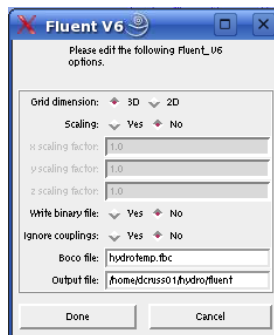
Figure 3.26: Output to Fluent menu

Meshing specific to Chapter 4:

The geometry for chapter 4 is simple. Use the tools presented above to create a tube 100m long, with a diameter of 0.60 m. Create a surface to partition the tube at 80m downstream. In Surface Mesh Setup, define the maximum size for the walls of the tube to be 0.1. For the inlet, outlet and partition surfaces, specify 0.03. In Global Mesh Setup, specify the scale factor to 0.9. Then, compute mesh.

Meshing specific to Chapter 5:

Geometries for chapter 5 are similar to those presented above for chapter 6, but on a smaller scale. The full 360 degree vessel is modelled, rather than the 180 degree section. Both vessels have a flat bottom, rather than a dish bottom. For the comparison with Rao (et al 1988), the vessel has a diameter and height of 0.56m. The impeller is a Rushton impeller with diameter 0.19m and clearance of 0.20. A partition surface should be created above the bottom at a height of 0.004m. The Global Element Scale Factor should be 0.049. Surface Mesh Setup parameters should be set as follows:

Side wall of tank – 0.75

Face of baffles – 0.75

Boundaries of inner zone – 0.75

Face of impeller blades – 0.5

Top/bottom of impeller disk – 0.5

Bottom of bottom zone – 0.1

Top of bottom zone – 0.11

For the comparison with Armenante (et al, 1998), the vessel diameter was 0.292m. The turbine was also a Rushton. The impeller diameter was 0.102m, the clearance was 0.117m. The false bottom partition was located 0.003m above the tank bottom. All scale factors were the same as for the Rao comparison.

3.4.4.2 Simulation setup

Load the Ansys Fluent program. In Fluent, go to *File -> Read -> Mesh*. When prompted, open the mesh file previously created. Fluent will take a minute or two to load the file. Once the mesh is loaded, use the *Mesh* menu to select *Smooth/Swap*. Alternately pressing *Smooth* Smooth and *Swap* Swap improves the quality of the mesh by rearranging nodes. Look for the results of smoothing or swapping in the display window on the bottom right. When neither smoothing nor swapping produces any change, press *Close* Close.
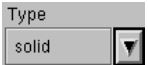
Most of the remaining navigation will be on the left menu. Choose *General* underneath *Problem Setup*. Press the *Units* button Units... on the *General* menu. Select 'Angular Velocity,' and change the default unit to 'RPM.' Press *Close*.

From the left menu, select *Materials*. The default fluid is set to 'Air.' Click on 'Air' and press *Create/Edit* Create/Edit.... In the textbox labeled 'Name,' change the name to 'PCS.' For 'Density,' input 1200. Press the drop down arrow ▼ next to 'Viscosity.' Select 'Herschel-Bulkley' from the drop down menu. Input 2.49 for the 'Consistency Index,' 0.715 for the 'Power-law Index,' 60 for the 'Yield Stress Threshold,' and 0.01 for the 'Critical Shear Rate.' Press *OK*, then *Change/Create*, then *Close*.
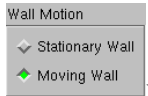
Now choose *Cell Zone Conditions* from the left. By default, all cell zones in Fluent are defined as fluid zones. In this simulation, however, only the zones INNER and
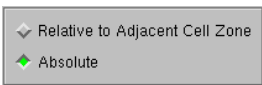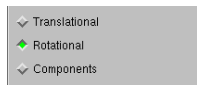
OUTER are truly fluid zones. The other zones need to be solid zones. This can be changed by selecting the drop down arrow below 'Type' and choosing 'solid.' Press *Yes* when prompted if the change is OK. This will bring up a menu to define the fluid zone. This same menu can be brought up by pressing the *Edit* button on the *Cell Zone Conditions* panel. Use this panel to specify for all zones (solid or fluid) a rotation axis origin of (0,0,0) and direction (0,1,0). For the moving zones (INNER, SHAFT, BLADE1, BLADE2, & BLADE3), change the 'Motion Type' to 'Moving Reference Frame,' and then set a 'Rotational Velocity' to 25 rpm.

Next, click on *Boundary Conditions* from the left menu. Select EXT from the list, and click the *Type* pull down arrow. Change the type to 'Interface.' Fluent will ask for permission to do so, then click *OK*. When it asks for a zone name, accept the current name EXT. Press *OK*. Do the same for EXT2, INT and INT2. The 'Interface' type allows for the application of non-conformal periodic boundaries, which will be applied in a later step. After setting the interfaces, change the type for BLEND to 'Interior.' Then, highlight the 'Impeller' boundary, press *Edit*, and it will bring up a large menu. Select the 'Moving Wall' radio button under 'Motion Type.' Then specify 'Absolute' motion , and then 'Translational' . Specify 25 for 'Speed (rpm),' (0,0,0) for 'Rotation-axis Origin,' and (0,1,0) for the 'Rotation-axis Direction.' Press *OK*. Then, with IMPELLER still highlighted, press *Copy* . Choose IMPELLER in the 'From Boundary Zone' list. Then, highlight all
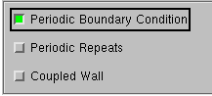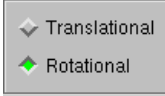
other boundaries with IMPELLER in the name in the 'To Boundary Zone' list (IMPELLER-SHADOW, IMPELLER:003, etc). Press *Copy*, and then press *OK*.

Return to the left menu, and click *Mesh Interfaces*. Click *Create/Edit*. Two mesh interfaces must be created, one to simulate periodic motion in the INNER fluid region, and one for the OUTER region. Enter the name 'IN' in the text box labeled 'Mesh Interface.' Highlight INT in the list below 'Interface Zone 1,' and then highlight INT2 in the list below 'Interface Zone 2.' Check the check box for 'Period Boundary Condition' . Then select the radio button for 'Rotational' . Uncheck 'Auto Compute Angle', and enter 180 into the 'Angle' box. Click *Create*, then repeat the process to create 'OUT' using EXT and EXT2. When the second interface is created, click *Close*.
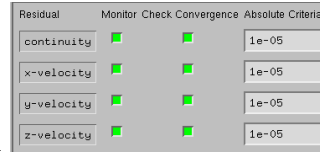
On the left menu, click *Reference Values*. Click the drop down arrow below 'Reference Zone' and select OUTER.

Choose *Solution Controls* from the left menu. Set the following 'Under-Relaxation Factors':

Pressure .2

Density .8

Body Forces .8

Momentum .2
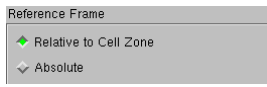
Now click *Monitors* from the left menu. Choose 'Residuals – Print, Plot' from
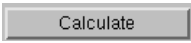
the top list, and click *Edit*. In the 'Equations' box , enter .0001

for the 'Absolute Criteria' for all residuals. Then press *OK*.
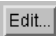
Click on *Solution Initialization* from the left menu. Be sure that 'Relative to Cell
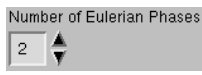
Zone' is checked in the 'Reference Frame' box . Then click .

Click *Run Calculation* on the left. Enter the desired number of iterations (2500 is

a good start). Then click *Calculate* .

Setup specific to Chapter 4

On the *General* menu, press the checkbox labeled *Gravity*. Specify (0,-9.8,0) for

the gravitational acceleration.

Select *Models* from the left hand menu. Highlight the top line, 'Multiphase – Off'

and press the *Edit* button . Click the radio button for 'Eulerian' and the menu will

expand. On the right hand side, use the arrow buttons underneath 'Number of Eulerian

Phases' to set 3 phases. Click *OK* to close the menu.

Next choose *Materials* from the left menu. Select 'Air' under the 'Fluid' heading

and then click *Create/Edit* . Change the name to 'oil' in the 'Name' textbox.

Change the density to 800 and the viscosity to 0.02. Then press *Change/Create*

 at the bottom. When asked about overwriting 'Air', select 'No' to create a

new material. Next, click *Fluent Database* on the right. In the list of

chemicals, scroll down to the bottom and highlight 'water-liquid (h20<l>).' Press the

Copy button Copy on the bottom, and then press *Close*. Press *Change/Create* again, and

then *Close* to close the menu.

After defining the materials, choose *Phases* from the left to assign materials to

different phases. Select the entry labeled 'phase-1 – Primary Phase' and press *Edit*.

Change the 'Name' to 'Water,' and then use the drop down arrow to change the 'Phase

Material' to 'water-liquid' Phase Material water-liquid ▼. Then press *OK*. Highlighting one

of the secondary phases and pressing *Edit* will bring up a more expansive menu. Change

the name to 'air' to indicate the oil phase and the size – 0.003. Select the last phase and

change the name to 'oil'.

Now return to the 'Models' tab. Select 'Population Balance Model' and choose

'Quadrature Moment' for the method. In the 'Phase' drop down, choose 'Oil'. Check

the checkbox for 'Phenomena', then check the boxes for 'Aggregation kernel' and

'Breakage kernel'. Select 'luo model' for each in the appropriate drop down. This will

define the drop size for the oil phase locally, dependent on flow conditions.

Next the user defined scalars (UDS) must be specified. In the top menu, choose

Define→User defined→Scalars. This will open the UDS dialog box. Use the arrows to

specify 3 for the Number of –User-defined Scalars. Uncheck 'Inlet Diffusion'. Use the

arrows next to move through the different scalars (0, 1 & 2). Using the drop box for

'Phase', specify one to the oil phase, one to the water, and one to the mixture. Press

'OK'.

Specify the inlet boundary to a velocity inlet. Specify the inlet velocity to 0.68

for each phase. Specify the inlet volume fractions for the oil and air phases to 0.03 and

0.02, respectively. Specify the inlet values for the UDS to zero. Specify the partition

boundary at 80m to an interior boundary.

In the Cell Zone Conditions tab, for each zone, check the 'Source Term' check

box, and define a constant source term of 1 for each UDS.

Lastly, under the Solution Controls tab, press the 'Equations' button. Deselect the

UDS. Run the simulation, return to the Equations tab, select only the UDS, then run the

simulation again. This allows for the MMA scalar to be calculated secondary to the

primary flow solution.

Setup specific to Chapter 5

Specify two materials – water and sand. Specify the density and diameter of the sand

phase according to the experimental conditions. Specify one UDS for the sand phase. In

the Cell Zone Conditions, specify a source term of 1 for the UDS in the bottom zone.

Specify a fixed value of 0 in the other two zones. When initializing the data, specify the

volume fraction for the sand phase according to the experimental condition.

3.4.4.3 Postprocessing

Data can be analyzed or extracted within the Fluent program. To find the torque, click on

Reports on the left menu. In the list, click 'Forces' and then select *Set Up…* .
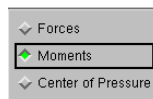
Highlight the radio button for 'Moments' . For the moment center, enter

(0,0,0) and the axis (0,1,0). In the list below 'Wall Zones,' select all zones with
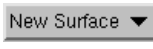
'IMPELLER' in the name. Then press *Print* . The torque will be displayed in the

output window on the right (Figure 3.27).

Figure 3.27: Example torque output

To view the flow field, choose *Graphics and Animations* on the left menu. In the top list box labeled 'Graphics,' choose 'Vectors' and press *Set Up….* Choose the *New Surface* button. This will open a drop down menu. On this menu, select 'Plane…'
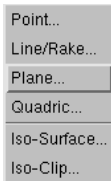
. This menu asks for three points, which will define a new surface. A convenient cross section of the tank can be viewed by inputting (0,0,0), (1,0,0) and (0,1,0). Name the new plane 'XY,' press *Create* , then press *Close*. Now, select 'XY' from the list box labeled 'Surfaces,' then press *Display* . If desired, the length of the vectors can be changed by changing the number in the 'Scale' text box. Also under the graphics and animations panel, contour plots can be generated using planes created above (Figure 3.28).

Average UDS values can be found in the Reports tab. Either surface integrals or volume integrals can be chosen to find the mean value across a surface or zone. The complete distribution can be found by exporting the data (File→export→solution data).
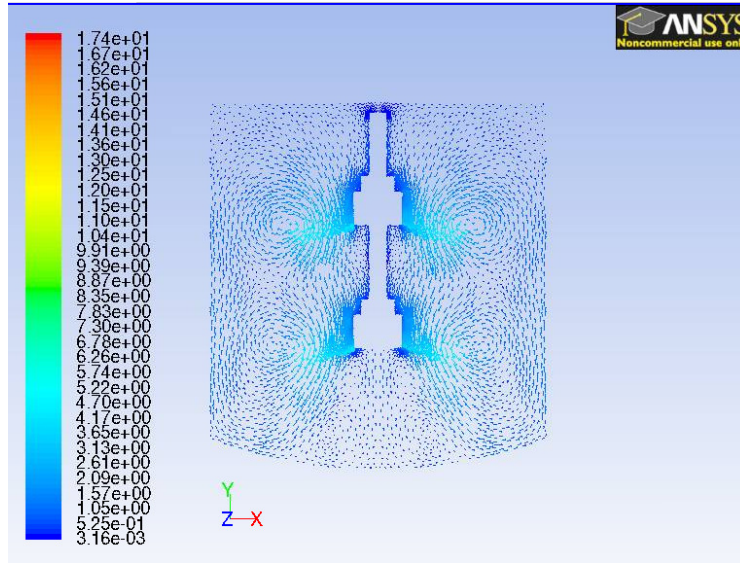
Figure 3.28: Example contour plot

CHAPTER 4. MEAN AGE THEORY FOR MULTIPHASE

The objective here was to develop a method for evaluating mixing quality by using multiphase mean age (MMA), and validate the method against experimental data and unsteady state CFD data. In the absence of comprehensive experimental spatial mean age distribution data throughout an entire system volume for multiple phases, a continuous oil/water flow system was chosen where RTDs were available at two points along the flow to use for validation (Sugiharto et al, 2009). MMA distributions were extracted as a subset of the spatial mean age contours determined from the model for each phase at both points of experimental measurement. Additionally, a simple liquid-solid (water-sand) system was simulated to demonstrate viability of MMA theory for different phase types.

4.1 MULTIPHASE MEAN AGE THEORY

Mean age theory as a means of modeling the time dependent behavior of a passive scalar in a steady-state CFD simulation has been derived elsewhere for a single phase system (Liu & Tilton, 2010; Sandberg, 1981; Spalding, 1958). The theory is extended here for application to multiphase systems. Liu & Tilton (2010) begin with the assumption that C(x,t) is the concentration of the scalar tracer at a given location x and time t, without further definition. It is reasonable to assume that their C(x,t) could be defined as:

$$C(x,t) = \rho \cdot \phi(x,t) \qquad (23)$$

where ρ is the density of the single phase and $\phi(x,t)$ is the scalar value at a given location

x and time t. The concentration of a passive scalar confined to a single phase in a

multiphase system can then be defined:

$$C(x,t) = \rho \cdot \alpha(x,t) \cdot \phi(x,t) \tag{24}$$

where $\alpha(x,t)$ is the individual phase volume fraction at a local position and time and ρ is

the density of the individual phase. With this definition of scalar concentration for

multiphase systems, the rest of the derivation proceeds analogously to that for a single

phase system (following Liu & Tilton, 2010).

Mean residence time for either definition of C can be defined as:

$$\bar{t} = \frac{\int_0^\infty t C_{out}\, dt}{\int_0^\infty C_{out}\, dt} \tag{25}$$

and can then be generalized to any point in the system by defining 'mean age' as:

$$a(x) = \frac{\int_0^\infty t C(x,t)\, dt}{\int_0^\infty C(x,t)\, dt} \tag{26}$$

This can be solved for any given point in the system. To do so, one must begin with the

transient passive scalar advection-diffusion transport equation:

$$\frac{\partial C}{\partial t} + \nabla \bullet (uC) = \nabla \bullet (D\nabla C) \tag{27}$$

Eqn. 12 and the derivation that follows are applicable to laminar flow systems. In a

turbulent system, Eqn. 12 can be replaced with the Reynolds averaging equation,

provided the time scale associated with turbulence is much smaller than the mean

residence time. In that case, D becomes the effective turbulent diffusivity and the rest of

the derivation transfers directly (Liu & Tilton, 2010). Multiplying both sides by time t

and integrating yields:

$$\int_0^\infty t\frac{\partial C}{\partial t}dt + \int_0^\infty \nabla\bullet(tuC)dt = \int_0^\infty \nabla\bullet D\nabla(tC)dt \tag{28}$$

The first term on the left can be integrated by parts to give:

$$\int_0^\infty t\frac{\partial C}{\partial t}dt = tC\Big|_0^\infty - \int_0^\infty C\,dt \tag{29}$$

Since for a pulse input in an open system it is known that:

$$\lim_{t\to\infty} tc = 0 \tag{30}$$

it can be inferred that:

$$\int_0^\infty t\frac{\partial C}{\partial t}dt = -\int_0^\infty C\,dt \tag{31}$$

Taking Eq. 9 and substituting it back into Eq. 6 gives:

$$-1 + \nabla\cdot\left\{u\left[\frac{\int_0^\infty tCdt}{\int_0^\infty Cdt}\right]\right\} = \nabla\cdot\left\{D\left[\frac{\int_0^\infty tCdt}{\int_0^\infty Cdt}\right]\right\} \tag{32}$$

Finally, substituting in Eq. 4 generates the age transport equation:

$$\nabla\bullet(ua) = \nabla\bullet D\nabla a + 1 \tag{33}$$

which can be expressed for incompressible systems as:

$$u\bullet\nabla a = \nabla\bullet D\nabla a + 1 \tag{34}$$

Both definitions of C produce the same transport equation, so the theory is now valid for

both multiphase and single-phase systems.

Boundary conditions for Eq. 12 have been derived elsewhere (Danckwerts, 1958;

Liu & Tilton, 2010) and are given as:

$$a = 0 \qquad\qquad\qquad \text{Inlet} \tag{35}$$

$$\frac{\partial a}{\partial x_n} = 0 \qquad\qquad\qquad \text{Outlet} \qquad\qquad\qquad (36)$$

$$\frac{\partial a}{\partial x_n} = 0 \qquad\qquad\qquad \text{Wall} \qquad\qquad\qquad (37)$$

where X_n is the normal direction. The outlet boundary condition has very little influence on the final result except when the Peclet number is very small (Froment & Bischoff, 1979). Additionally, strictly speaking the inlet should be a single inlet which is uniform in regards to inlet velocity and age.

4.2 CFD MODELING

CFD models were created to simulate an oil-water flow system for which residence time distributions were available at multiple locations (Sugiharto et al, 2009). The system consisted of a 100m length of pipe with a diameter of 61cm that contained water, oil, and air at volume fractions of 95%, 3%, and 2%. The operating temperature was 70°C. Residence time distributions were measured for the water and oil phases only at 80m and 100m. CFD simulations of this system were performed with ANSYS Fluent, v 14. Unstructured meshes with tetrahedral cells were generated using ANSYS ICEM. The three dimensional mesh contained 1 480 405 cells. Optimal mesh count was determined based on a sensitivity analysis of mean residence times and variances across a range of 307k-1 711k cells. The primary phase was water, while crude oil and air were the secondary phases. Multiphase behavior was simulated using a Eulerian multiphase model. Drop size distribution to account for the oil phase behavior was modeled using the population balance model, and its six moments were calculated according to the quadrature method of moments. Bubble sizes for the gas phase did not have a significant impact on the results, and so they were held constant. Aggregation and breakage were

modeled by the Luo model. For the granular solid phase, granular viscosity was modeled

according to Syamlal and O'Brien (1989). Granular bulk viscosity was modeled

according to Lun, et al (1984). Phase drag interactions were modeled according to Ding

& Gidaspow (1990). Turbulence was simulated by the standard k-e model. For steady-

state results, the CFD solver computed the scalar values, a(x), using MMA theory

(Equation 12) after the steady-state flow solution was obtained. For transient results, the

flow field and scalar solutions from the advection-diffusion equation (Equation 5) were

solved simultaneously.

4.3 SPATIAL DISTRIBUTIONS

Contour plots of age across a cross section of the flow at 80m demonstrate how MMA

theory integrated with CFD provides comprehensive spatial variation in mean age for

each phase. The three images show independently the age distribution for the overall

mixture (Figure 4.1a), the water phase only (Figure 4.1b), and the oil phase only (Figure

4.1c). The contours in Figure 4.1a and 4.1b are nearly identical to each other, due to the

very high phase fraction of water in the system, while the mean age distribution of the

secondary oil phase in Figure 4.1c differs significantly. The concentration of age at the

top of the pipe represents the oil having risen to the top due to buoyancy. The value

displayed on the contour throughout most of the pipe cross section is zero since no scalar

transport will occur where there is no secondary phase present. The ability to distinguish

mean age distributions for each phase independently, and therefore identify local mixing

characteristics for each phase independently, provides new critical knowledge for which a

number of diverse applications, particularly at very long time-scales, are envisioned such

as: understanding and modeling pollutant dispersion in the atmosphere, streams and
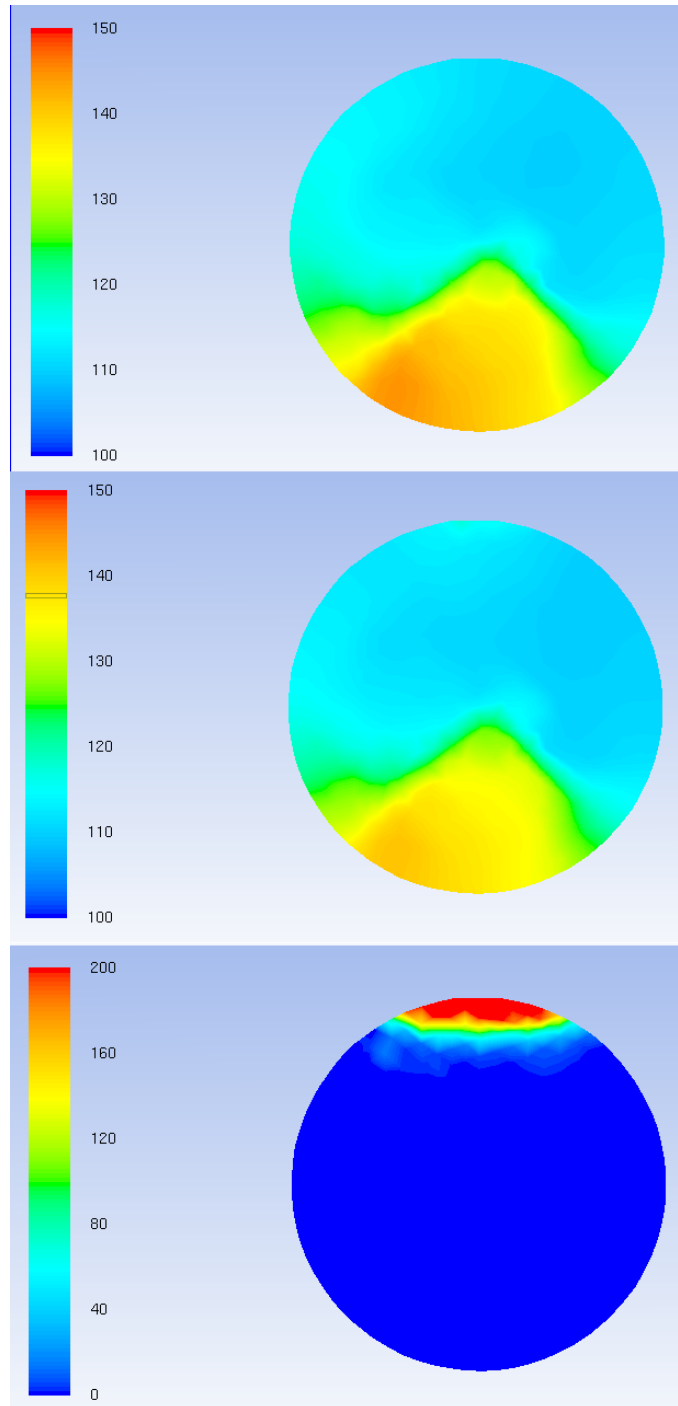
Figure 4.1: Cross section of age contours at 80m for a) mixture, b) water phase only, and c) oil phase only. Oil contour shows zero value where no oil is present.

oceans; many biomedical applications such as modeling and predicting platelet settling in

human vascular system and identifying drug or chemical dispersion in organs; and

predicting reaction yield for heterogeneous reactions.

4.4 MMA DISTRIBUTIONS

Mean age distributions were extracted from the solutions to compare to both the experimental RTD measurements as well as to a conventional transient solution. Mean age distributions are expected to be somewhat narrower than residence time distributions, since the values have been averaged (*mean* age). However, in perfect plug flow conditions, the two should be identical. In conditions approaching plug flow, such as flow through a pipe, the results should be similar, though the MMA distribution will usually have a shorter tail.

Figure 4.2 shows the MMA distributions for each phase at 80 m and 100 m. Both
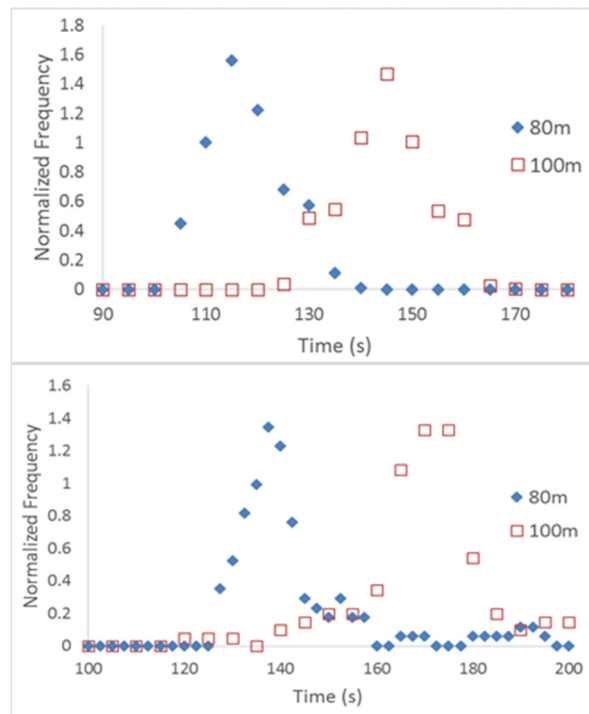
Figure 4.2: Frequency normalized mean age distributions
for a) water and b) oil, generated by MMA theory.

the water phase (Figure 4.2a) and the oil phase (Figure 4.2b) exhibit a peak and tail pattern. The tail shows more prominently on the oil phase, due to greater mixing

associated with the secondary phase. The curves are consistent with RTDs that display

the general form of a tanks-in-series model fitting.

4.5 COMPARISON WITH EXPERIMENTAL RTDS

MMA distributions matched very well visually to experimental measurements

(Figure 4.3), which was quantitatively confirmed in Table 4.1. The mean residence times
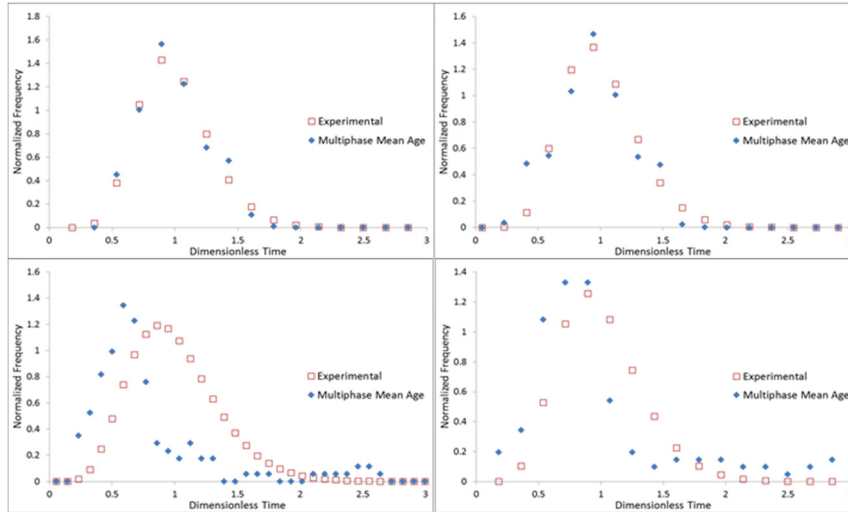
Figure 4.29: Comparison of MMA/RTD between MMA theory and experimental data for a) water at 80m, b) water at 100m, c) oil at 80m, and d) oil at 100m. Experimental values from Sugiharto et al.

for the water phase differed by less than 1% at both locations. Variances differed by

~8% (80m) and 3% (100m). Mean residence times for the oil phase both differed by

~3%, and variances by 10% (80m) and 5% (100m). Variances were calculated based on

the primary peak and did not consider the full length of the tail, since the MMA

distribution was known to be shorter. Visually, the biggest discrepancy was for oil at

80m, which shows a departure on the tailing edge, but the leading edge matches almost

perfectly. Overall, these are very reasonable differences for a numerical result.

Numerical models such as turbulence or breakage and coalescence models can account

for a several percent difference between simulation and experiment. Common

69

experimental error, such as inaccuracies with tracer injection and measurement might

also account for some of the differences.

4.6 COMPARISON WITH TRANSIENT CFD RTDS

Steady-state MMA distributions were compared to conventionally derived

transient RTDs (Figure 4.4 and Table 4.1). Steady and transient derived mean
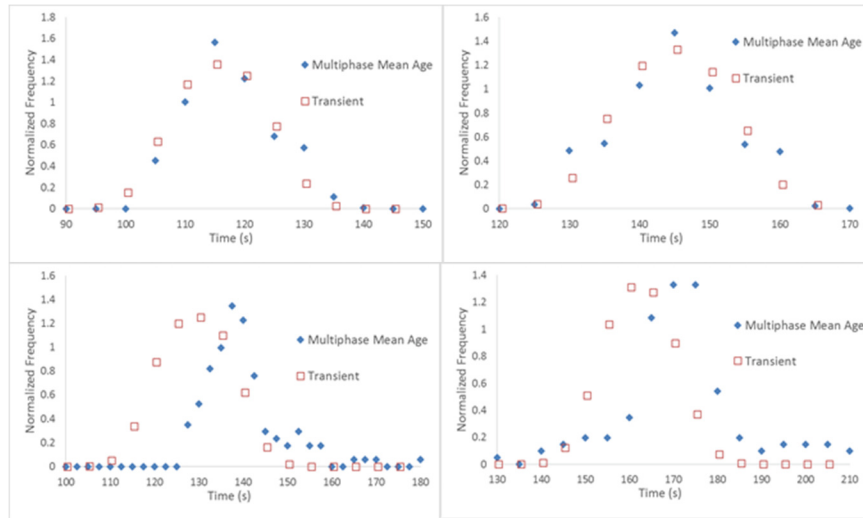
Figure 4.4: Comparison of MMA/RTD between steady and transient CFD for a) water at 80m, b) water at 100m, c) oil at 80m, and d) oil at 100m.

residence times for water at 80m (Figure 4.4a) and 100m (Figure 4.4b) were identical.

Distribution variances differed by 4% at 80m and 14% at 100m. There was a slight offset

between the oil phase distributions (Figures 4.4c and 4.4d), but mean residence times

were still within 8% and 4% of each other. The greater deviations in the mean residence

times of oil are attributed to the small phase fraction for the oil. Since the system is

water-dominated, the modeled flow behavior of the oil will be more susceptible to minor

computational discrepancies, with a small difference producing a larger percent

deviation. Distribution variances for the oil phase differed by 11% (80m) and 13%

(100m).

Table 4.1: Mean residence times and variances determined from MMA theory steady-state solution, transient solution, and experimental measurements. Experimental data from Sugiharto et al.

Water 80m	MRT	Variance	MRT Difference (From MMA)	Variance Difference (From MMA)
Multiphase Mean Age	118	0.0440	-	-
Unsteady CFD	118	0.0424	0.000	-0.0366
Sugiharto et al, 2009	119	0.0405	0.00848	-0.0791
Water 100m	MRT	Variance	MRT Difference	Variance Difference
Multiphase Mean Age	147	0.0273	-	-
Unsteady CFD	147	0.0309	0.000	0.134
Sugiharto et al, 2009	146	0.0265	-0.00680	-0.0274
Oil 80m	MRT	Variance	MRT Difference	Variance Difference
Multiphase Mean Age	144	0.0516	-	-
Unsteady CFD	133	0.0457	-0.0764	-0.115
Sugiharto et al, 2009	149	0.0465	0.0347	-0.0992
Oil 100m	MRT	Variance	MRT Difference	Variance Difference
Multiphase Mean Age	173	0.0607	-	-
Unsteady CFD	166	0.0530	-0.0405	-0.127
Sugiharto et al, 2009	178	0.0577	0.0289	-0.0497

The transient solution produced smoother RTDs than the steady solution since the transient computations experience a temporal fluctuation, while the steady computations experience a spatial fluctuation. The transient tracer updates with each time step, creating a temporal fluctuation, but the actual measurement at each time step is a mass weighted average across the entire cross section, and so any spatial variation is averaged out. Conversely, for the multiphase mean age results, there is no temporal fluctuation,

due to the steady-state simulation. Rather, the mean age distribution comes from fluctuations in value at different points on the cross section. The distribution is measured by taking a histogram of these results, so spatial variation is essential to the measurement.

The steady-state model appears to be more accurate than the transient model since the MMA derived mean residence times and variances more closely match the experimental data than do the transient derived values. Transient solutions inherently introduce more error due to the dependency on time step size as another variable. A small error introduced at an early time step, such as modeling the tracer injection, can propagate throughout the rest of the solution. While both the steady and transient solutions gave equal mean residence times for water at both locations, the steady MMA solution mean residence times were closer to the experimental values for the oil phase at both locations. The experimental mean residence time for oil at 80m was 149 seconds; the steady solution gave 144 and the transient gave 133. The experimental mean residence time for oil at 100m was 178 seconds; the steady solution gave 173 and the transient gave 166. Transient solution variances were also closer to the experimental values for three out of the four cases. The experimental variance for water at 80m was 0.049; the steady solution gave 0.044 and the transient gave 0.042. For water at 100m, the experimental and steady solution values were both equal to 0.027, while the transient solution value was 0.032. Oil at 80m was the lone exception where the transient value matched the experimental value at 0.046, while the steady solution value was 0.052. At 100m, the experimental variance was 0.058, the steady variance was 0.061, and the transient variance was 0.53.

4.7 MMA IN A LIQUID-SOLID SYSTEM

MMA theory was applied to a hypothetical 90% water / 10% sand mixture to demonstrate the versatility of the technique towards different phase types (Figure 4.5).
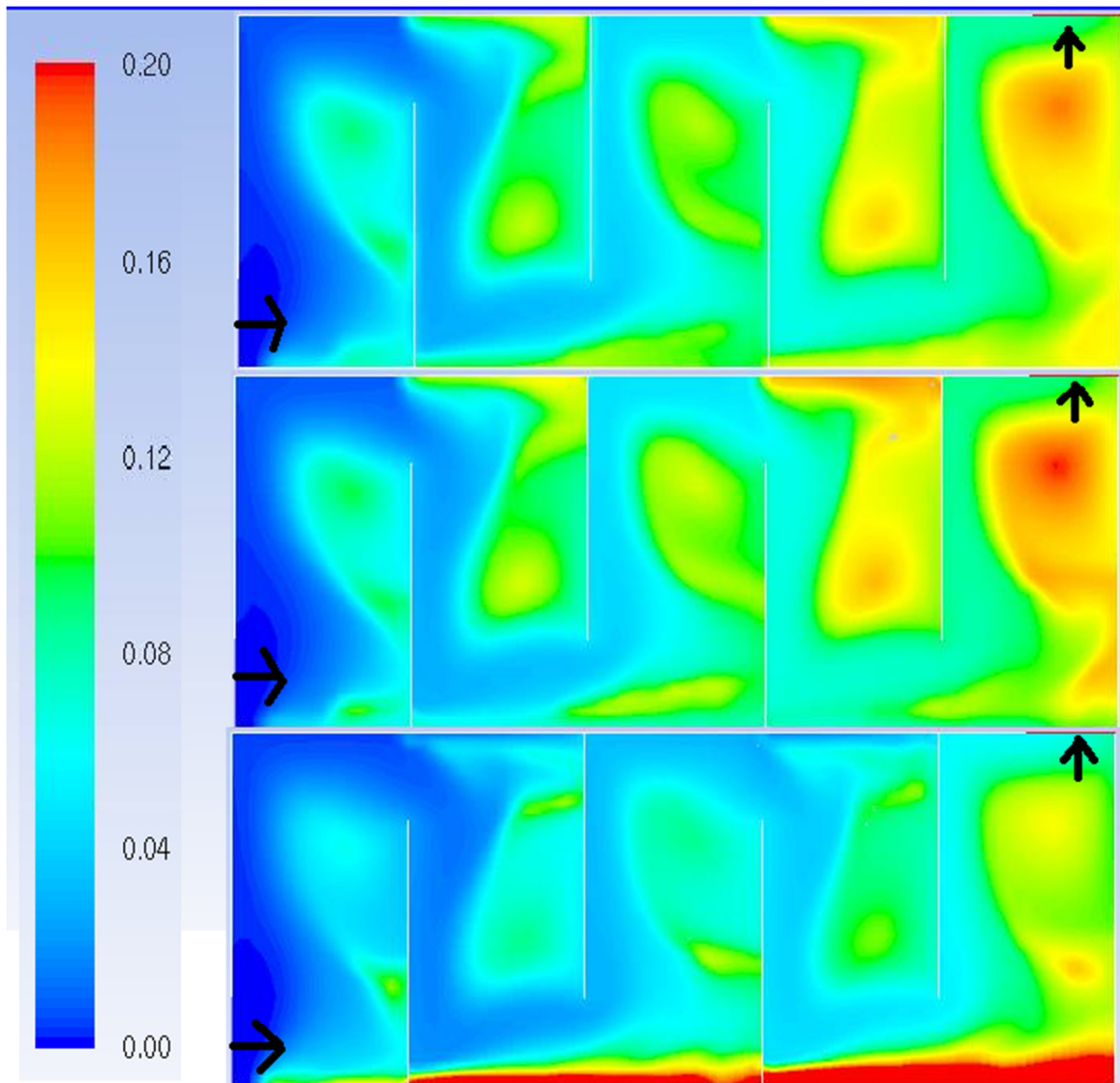
Figure 4.5: Contours of age for a) mixture, b) liquid phase only, and c) solid phase only for a water-sand mixture. Arrows indicate direction of flow at inlet and outlet.

The snaking geometry of this system highlights how mean age differs between the primary and secondary phases. The solid phase is expected to exhibit some settling behavior, which appears in this type of analysis as higher age. Figure 4.5a shows the age of the mixture, Figure 4.5b shows the age of the water phase, and Figure 4.5c shows the

age of the sand phase. As in Figure 4.1, the ages of the overall mixture and water appear to be nearly identical to each other due to the high fraction of water. However, the bottoms of the second and third compartments show high concentrations of age, particularly at the bottom of columns where the mixture is flowing downward, indicating settling of the sand due to its higher density. Residence time distributions, even if measured independently for each phase, are more limiting in that they do not reveal the spatial distribution, which is clearly advantageous as demonstrated here. In its current form, MMA is only applicable in systems with immiscible phases, such as water-oil or water-sand.

4.8 Summary

A new theory was developed for determining spatial and temporal mean age distributions for each phase independently in multiphase systems. The theory requires defining the concentration of a passive scalar in terms of the density and volume fraction for each phase at every location over time. The theory was well validated by simulating mean age distributions for water-oil flow in a pipeline. Mean residence times generated computationally by MMA theory were within 1% of experimental values for the primary water phase and 3% for the secondary oil phase. MMA curve variances differed by 3-11% between the computational and experimental RTD results. Means and variances of the new steady-state MMA method matched experimental values more closely than did the conventional transient computations, indicating better accuracy due to the steady-state solution. MMA theory provides a substantial improvement over traditional RTDs since it provides age distributions over space and volume rather than just at discrete locations, plus it is more computationally practical for applications with very long time scales. The

technique demonstrated versatility with application to both liquid-liquid and liquid-solid multiphase systems, and should be easily extendable to systems involving gas phases as well, allowing for a wide variety of applications including pollution modeling, fluidized beds, sedimentation modeling, and cardiovascular applications, among many others.

CHAPTER 5. COMPUTATIONALLY DETERMINED JUST SUSPENDED SPEED USING MULTIPHASE MEAN AGE THEORY

Multiphase mean age theory (MMA) was applied here to obtain local, time dependent data for solids in proximity to the bottom of mixing vessels. The objective was to apply the multiphase mean age technique towards a novel approach for predicting just suspended speed. This was accomplished by validating the technique by comparing computational and experimental just suspended speed across a range of solid densities, solid fractions, and particle size.

5.1 MMA ZONE DEFINITIONS FOR LOCALIZED ANALYSIS

Because MMA gives time related data, the technique described in Chapter 4 can be extended to analysis of just suspended speed. At its most basic definition, just suspended speed is dependent on the time solids spend in proximity to a vessel bottom, up to 1-2s (Zwietering, 1958). Model zone definitions can be applied in conjunction with MMA to allow specific analysis in regions of interest within a vessel. Figure 5.1 shows an example of such conditions for examining settling and N_{jss} in a mixing tank. Zone A was set as a rotating reference frame to adequately accommodate impeller motion for the purpose of modeling. Zones B and C were set as stationary zones in the modeling. Zone C exists solely for determining the age in the bottom of the vessel. The age transport equation is not solved in Zones A or B, while mean age follows the mean age transport equation, Equation 4, in Zone C. The height of Zone C is on the order of 1% of the total height of the vessel, since only the behavior at the very bottom is relevant for determining
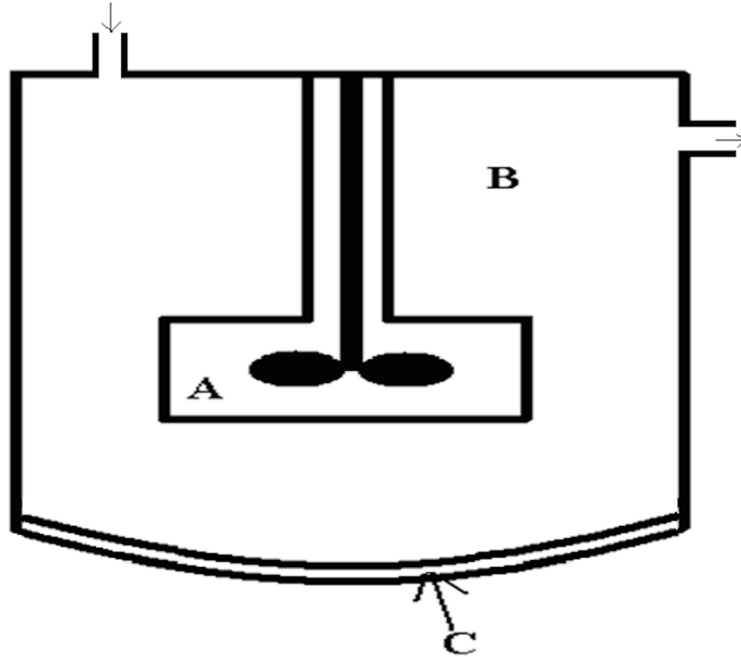
*Figure 5.1: Diagram of zone selection for measuring
N_{jss}. A is a moving reference frame, B is a
stationary zone, and C exists for measuring age near
the vessel bottom.*

N_{jss}. The thinner this zone the better, though a lower limit may be reached due to particle

size or meshing concerns. The ratio of zone height to particle diameter used here ranged

from 15:1-60:1.

A scalar measurement confined to the solid phase in Zone C will measure the

local residence time of a solid particle in close proximity to the bottom. If the particle is

suspended (residing anywhere above Zone C), then the age there will be relatively low

since the transport of the scalar will be convection dominated. However, if the particle is

settling (in Zone C), then convective transport of the scalar will go to zero while slow

diffusive transport will dominate, which will generate higher order of magnitude age

values. Figure 5.2 shows a theoretical result for such a condition. Each point represents

the average of the MMA in Zone C for a given impeller speed. Above N_{jss}, the age value
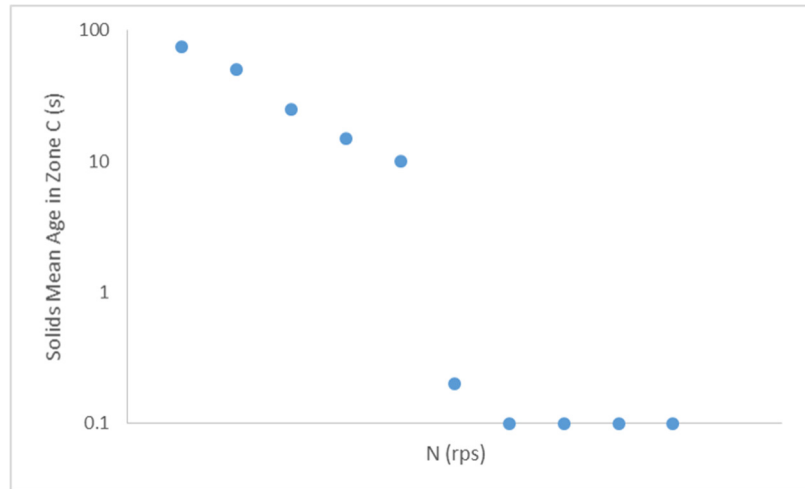
Figure 5.2: Theoretical age of solids in Zone C for varying impeller speed. Above Njss, age is low and steady due to convection dominance. Below Njss, age is much higher, due to the absence of convection. The sharp transition marks Njss.

is very low. Below N_{jss}, the age value is orders of magnitude higher. N_{jss} occurs at the discontinuity between the two regions of the graph. The transition from convection-dominated transport to diffusion-dominated transport as impeller speed decreases results in a very sharp increase in age.

5.2 CFD MODELING

CFD simulations were performed with ANSYS Fluent, v 14. Impeller motion was modeled using multiple reference frames. Unstructured meshes with tetrahedral cells were generated using ANSYS ICEM. All models contained between 450,000-500,000 tetrahedral cells. Mesh density was refined along the vessel bottom, in the bottom zone. Mesh sensitivity was performed, beginning with a total mesh count of 90,000 cells. The cell count was increased by a ratio of 1.5 per mesh iteration, while the average mean age in the bottom region was tested. Mesh insensitivity was reached after 5 mesh iterations. The liquid phase simulated was pure water. The solid phase simulated was sand or resin particles with varying diameters and densities. Multiphase behavior was simulated using

a granular, Eulerian model. Turbulence was modeled using the RNG k-e model.

Granular viscosity was modeled according to Syamlal and O'Brien (1989). Granular

bulk viscosity was modeled according to Lun, et al (1984). Phase drag interactions were

modeled according to Ding & Gidaspow (1990). Flow solutions were obtained first, then

the scalar tracer values were computed from the resulting steady state flow field.

5.3 OPEN VS CLOSED SYSTEM RESULTS

The method introduced here modifies the inlet and outlet boundaries which are

typically applied towards mean age (Liu & Tilton, 2010). The boundaries used here

apply solely to the bottom of the vessel, Zone C, which is the region of interest. Figure

5.3 shows the boundary at the top of Zone C. Anywhere the z-velocity is negative, the
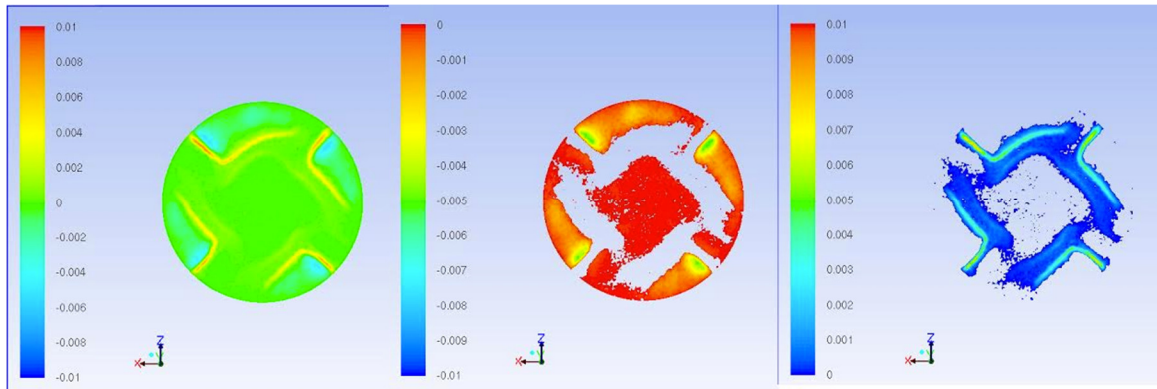
Figure 5.3: Contours of vertical velocity along the boundary between zones B & C. Negative velocity indicates an inlet to zone C, while positive indicate an outlet from zone C.

flow is into Zone C and the region can be viewed as an inlet. Anywhere the z-velocity is

positive, the flow is out from Zone C and the region can be viewed as an outlet. Outlet

boundaries are known to have a very weak effect on mean age.

For the boundaries defined here to be considered valid, the method must predict

the same Njss as a conventional open system. Figure 5.4 shows results for a sand-water

79
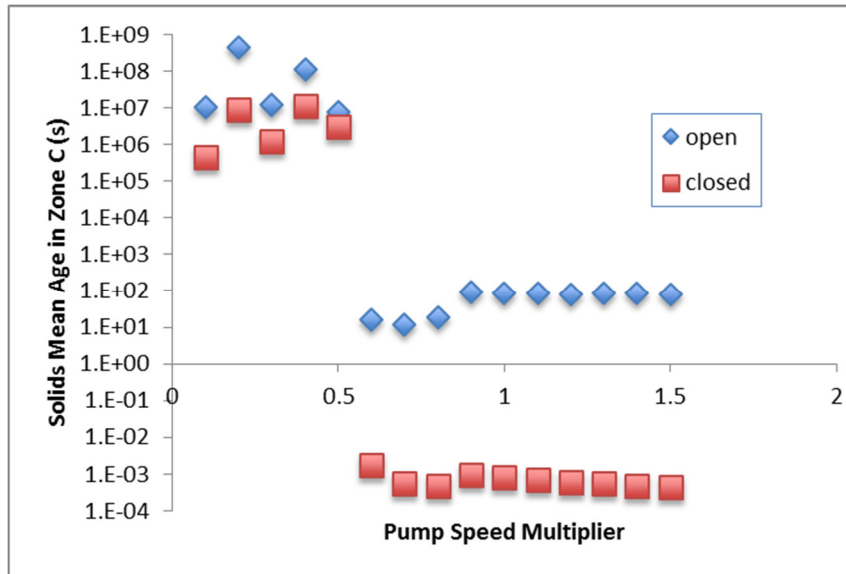
Figure 5.4: Comparison of mean age of solids between the open and closed systems. Both techniques predict the same Njss.

system in a 97 cm, stirred tank with H/T=1, an axial flow impeller, and particle size of 111 μm. The tank is a true open system with flow in through an inlet and flow out through an outlet. For the "closed" system, the boundary conditions at the tank inlet and outlet were specified to be no flux. For the true open system, the flow rate was chosen arbitrarily low, to give a mean residence time on the order of 1000 s. Further, the age transport equation was solved in all zones in the true open system, including Zones A and B, since flow entered through a traditional tank inlet. Since the closed vessel had a smaller region where the scalar was calculated (in Zone C only), the magnitude of the values is smaller, but most importantly, the order of magnitude increase in age, which predicts N_{jss}, occurs at the exact same agitation speed, validating the assumptions. Clearly the "closed" system predicted N_{jss} just as well as the true open system, and with the added benefit of isolating precisely the area of interest.

5.4 PREDICTION OF JUST SUSPENDED SPEED AND COMPARISON TO EXPERIMENTAL RESULTS

80

To highlight the usefulness of this technique, simulations were run to predict just suspended speed (N_{jss}) for a variety of liquid-solid systems. Referring again to Figure 5.4 shows sample results obtained using the technique. As predicted by Figure 2, age values above N_{jss} are relatively constant and low, consistent with a convection-dominated system in the bottom region where particles have not settled. Below N_{jss}, the values are ~4-6 orders of magnitude higher, consistent with a diffusion-dominated system due to the presence of settled solids. At N_{jss} there is a significant discontinuity between the two regions, which corresponds with the speed above which all particles are at least just suspended, and below which some are not suspended. While there is some noise present below N_{jss}, the trend is indisputable, and the noise ceases sharply at N_{jss}. Above that speed there is no noise on the order of magnitude seen at slower impeller speeds. These results are in keeping with the predictions from Figure 5.2.

Two published studies were used for experimentally validating this computational N_{JSS} method for a range of solid densities, solid fractions, and particle sizes (Armenante et al, 1998; Rao et al, 1988). These selections also allowed for testing the technique across multiple tank and impeller sizes and geometries. The technique was tested for a range of solid densities between 1375-2500 kgm^{-3} (Figure 5.5). Two of the density values used for validation were actual experimental data (Armenante et al, 1998), and two were values calculated from a correlation presented in the same publication. The correlation was used for additional validation in lieu of more experimental data since density could be easily altered this way while holding all other particle properties
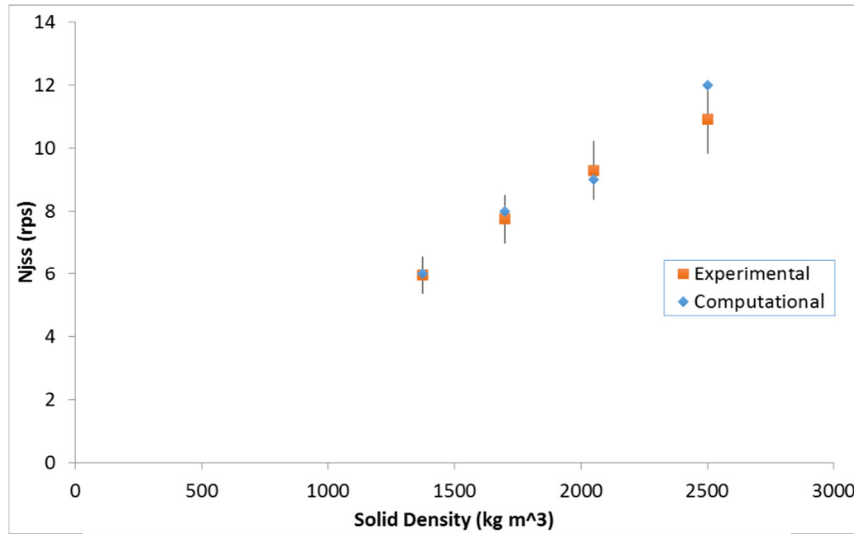
Figure 5.5: Njss as a function of solids density.
Experimental data from Armenante et al. (1998).

constant. N_{jss} determined computationally based on MMA deviated from the
experimental data/correlation by an average of 3%. When varying the solids
concentration between 0.6%-12% and using a pitched blade turbine, computationally
determined N_{jss} deviated from published experimental results by an average of just 3%
(Figure 5.6). The solids concentrations tested represent a wide range of concentrations
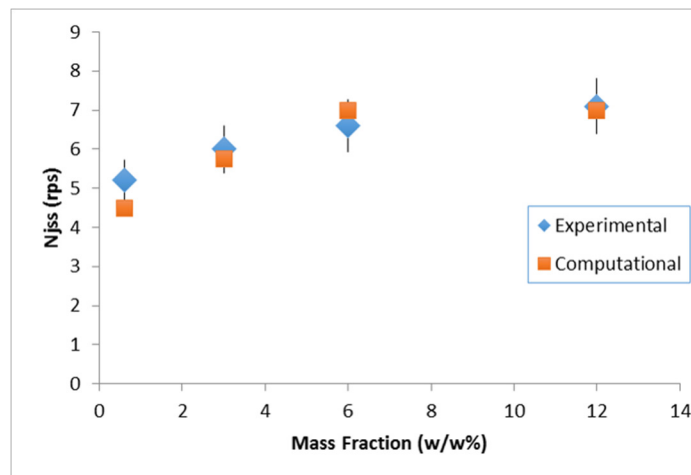
Figure 5.6: Njss as a function of mass fraction.
Experimental data from Rao et al. (1988)

from both laboratory and industrial applications. Figure 5.7 shows a comparison to
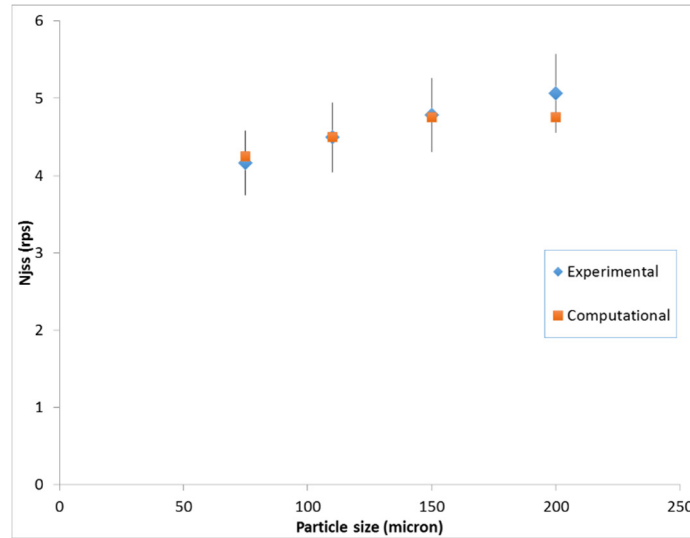
Figure 5.7: Njss as a function of particle diameter.
Experimental data from Armenante et al (1998)

experimental results across a range of particle sizes and with a different system geometry than the data in Figure 5.6. When varying the solid particle size from 75-200 μm and using a Rushton turbine, computationally determined N_{jss} deviated from experiments by an average of just 1%.

The very close agreement between computational and experimental results indicates that the technique is robust across a wide range of conditions. This also provides further evidence that the modified boundaries are empirically accurate. Any discrepancy between this technique and experimental results may be attributed as much to difficulties inherent in experimental measurements as it is to computational accuracy. The overall deviation is 3% or less, which is similar to the error reported in Zwietering's (1958) foundational study (2-3%), and given the continued widespread use of Zwietering's method, it is reasonable to conclude the error in this study is on par with that reported elsewhere.

5.5 Summary

A new technique has been developed for accurately applying MMA theory towards predicting the just suspended speed in mixing tanks. A closed system with modified boundaries generated results as reliably as the rigorous open system. The multiphase mean age technique was shown to accurately predict N_{jss} across a range of solid densities, solid fractions, and particle sizes with average deviation from published experimental data of just 1-3%. Furthermore, tests were performed in different size tanks with different impeller types indicating accuracy across a range of scale and geometries. This steady state CFD technique can predict just suspended speed results with less computational time compared to unsteady CFD methods, with error equivalent to experimental methods, and without inherent experimental drawbacks such as altering the flow regime, requiring transparency, or subjective experimental variability.

CHAPTER 6. PREDICTING POWER FOR A SCALED-UP NON-NEWTONIAN

BIOMASS SLURRY

The objective was to evaluate the effect of scale and rheology on power number in high solids biomass slurries. Pretreated corn stover slurry was studied in a 3.8 million L reactor using conventional mixing impellers. Because it was impractical to test on an actual reactor of this size, computational fluid dynamics (CFD) was employed using a model validated against laboratory-scale data. The scaled-up model was compared against experimental and simulated lab-scale data to determine the effect of scale and geometrical arrangement on power number for non-Newtonian biomass slurry with a yield stress operating in the transitional flow regime.

6.1 CFD MODELING

CFD simulations were performed with ANSYS Fluent, v. 12. Impeller motion was modeled using multiple reference frames. The slurry was modeled as a single-phase Herschel-Bulkley fluid. Rheology data were fit to the Herschel-Bulkley model (Eqn 9), and the corresponding parameters were determined to be yield stress $t_y = 60$ Pa, consistency index $k = 2.49$ kg m^{-1}s^{-1}, and power law constant $n = 0.715$. Unstructured meshes with tetrahedral-shaped cells were generated with ANSYS ICEM. Laboratory-scale models used for validation contained approximately 509 000 cells. Sensitivity analysis was performed on the industrial-scale meshes, using torque on the impeller as the measurement criterion. A change from 1 million to 1.5 million cells produced a

change of 0.3 %, indicating the solution was grid-independent. However, to be conservative, the 1.5-million-cell mesh was used.

The laminar flow model was employed for the CFD validation. The range of Reynolds numbers for the transition region in stirred tanks is wide, i.e., 10–10 000. Calculating a Reynolds number for mixing in non-Newtonian systems is necessarily an approximation, since viscosity varies spatially according to the flow pattern. Reynolds numbers based on the Metzner-Otto method indicate that all tested cases are in the transition regime, and many were at the lower end of that range. Transitional flow behavior for non-Newtonian fluids is relatively unknown compared to Newtonian systems, and it is known that these systems will often never reach a fully turbulent condition (Ghotli et al, 2013). Consequently, in the transition region, portions of the tank will exhibit laminar flow, while others may reveal turbulent flow. Given the high yield stress of the system, a large amount of shear is required to even achieve laminar motion, and so much of the fluid away from the impeller will not have reached a fully turbulent state. This heterogeneous flow can be difficult to model with either a laminar or turbulent model (Tatterson et al, 1994). A validated laminar model was compared against a turbulent model.

Following validation, the CFD model was scaled up to 3.8 million L. All of the model parameters remained the same. The vessel diameter (T) was 17.5 m, with a dish-bottom. At this scale, a 45 degree PBT and an A310 hydrofoil were tested. These were chosen as they are widely used, even in non-Newtonian systems, and can provide a baseline impeller setup (Bujalski et al, 1999; Guntzberger et al, 2013; Wu, 2012). Additionally, since these impellers can function in both Newtonian and non-Newtonian

regimes, they can be used in enzymatic hydrolysis reactions where the rheology of the slurry changes drastically during the course of the reaction where the solids content starts high and ends low. Two impeller diameters (D) were tested, 1/3 T and 1 /2 T. Impeller clearance (C) was tested at 1/3 T and 1 /2 T. Impeller speeds were chosen such that the corresponding tip speeds equaled those from the validation vessel. Since the Reynolds numbers for the system were in the transition region, a laminar model was compared against the RNG k-e turbulence model, which is well respected for modeling the transition regime (Bakker, 2006). Additionally, there is precedence for using the RNG k-e model in non-Newtonian systems (Chen et al, 2009; Gunyol & Muddle, 2009), including transitional flows (Niezgoda-Zelasko & Zalewski, 2006), which would exhibit heterogeneous behavior. The large Eddy simulation model may better resolve the turbulence for heterogeneous flow, but the computational cost is orders of magnitude higher owing to the requirements of an even finer mesh, especially at this million gallon scale, and unsteady state solution.

6.2 MODEL VALIDATION

6.2.1 Power Number at Lab-Scale

The test for validation was comparison of torque required to turn the shaft between that measured in the actual 2 L vessel and CFD model predictions. Torque was within the experimental margin of error, indicating good validation for the CFD model. The power number (Eqn 11) for a PBT in a fully turbulent Newtonian system, regardless of rheology or geometry, is 1.5. The power number obtained for this system, both experimentally and computationally using the laminar model, was 0.25 (Fig. 6.1b).

Reynolds numbers Re in Fig. 6.1b were calculated using the method of Metzner and Otto
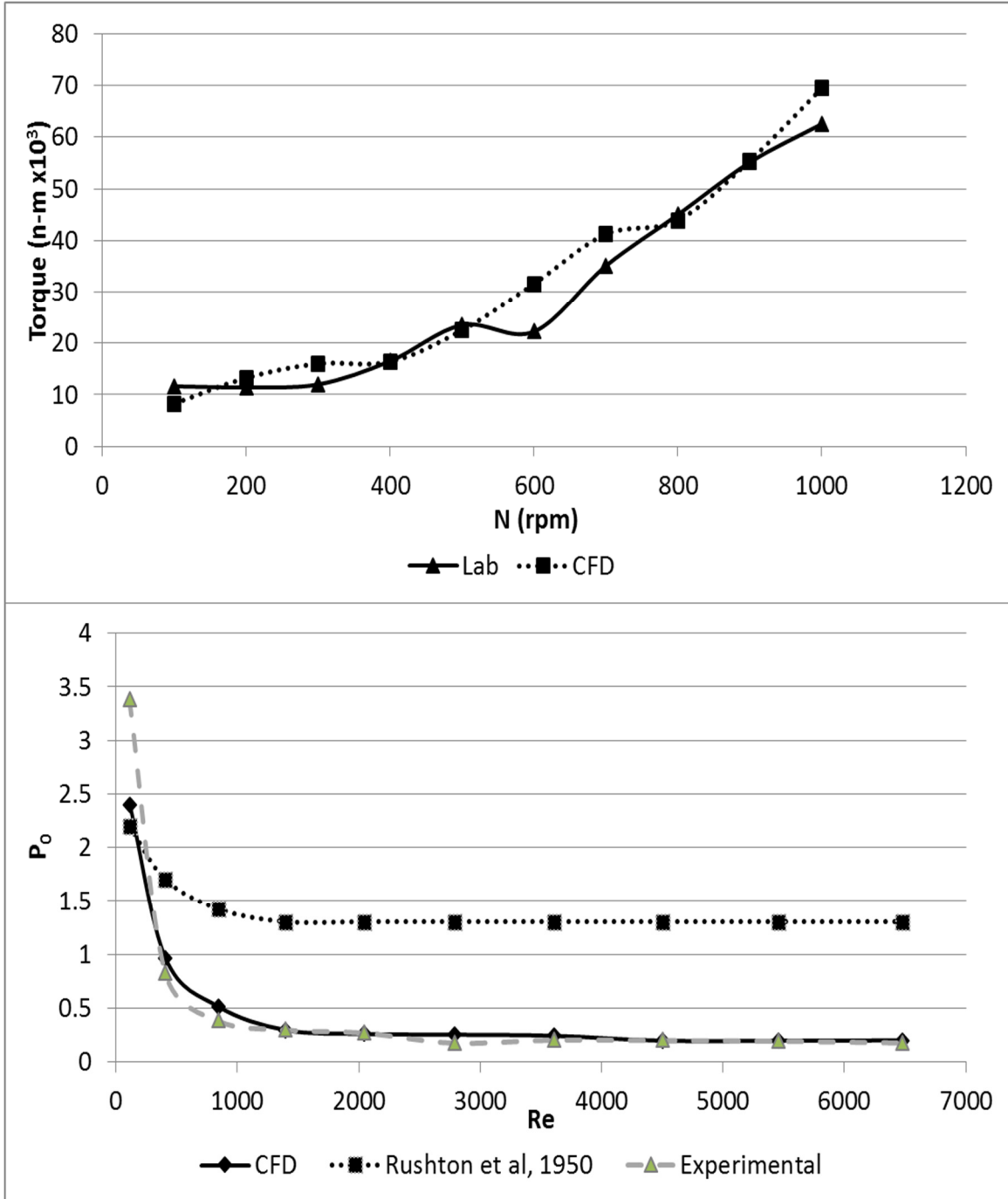
Figure 6.1: (a) Comparison between computational and experimental torque; (b) power number vs. Re in the laboratory-scale vessel, compared with pitched-blade data from Rushton et al. 1950. Error bars indicate fluctuations on the torque sensor.

(1957). The lower power number is indicative of the non-Newtonian rheology of a fluid

compared for impeller speeds between 100 and 1000 rpm (Fig. 6.1a). The model data fit

in transitional laminar-to-turbulent flow affecting the flow patterns in the vessel. The

yield stress means less fluid is in motion, particularly away from the impeller, and

therefore less power was applied. It has been reported elsewhere that power numbers in

the transitional regime can deviate below Newtonian values (Nienow & Elson, 1988). At

Re = 400–1600, the system exhibits a clear change from laminar flow, characterized by a

downward linear trend with Re, to turbulent flow, which has no dependence on Re. This

transition occurs when turbulent flow patterns tend to dominate the power draw more

than laminar flow patterns. This does not necessarily mean the vessel is fully turbulent,

only than it is partially turbulent. Heterogeneous flow can still be expected, with some

regions behaving laminar, and others turbulent. Transitional flow can be expected for Re

higher than this specific critical Reynolds number (Peixinho et al, 2005).

6.2.2 Cavern Measurements

A second test for validation was accurate prediction of the cavern depth (Fig 6.2)
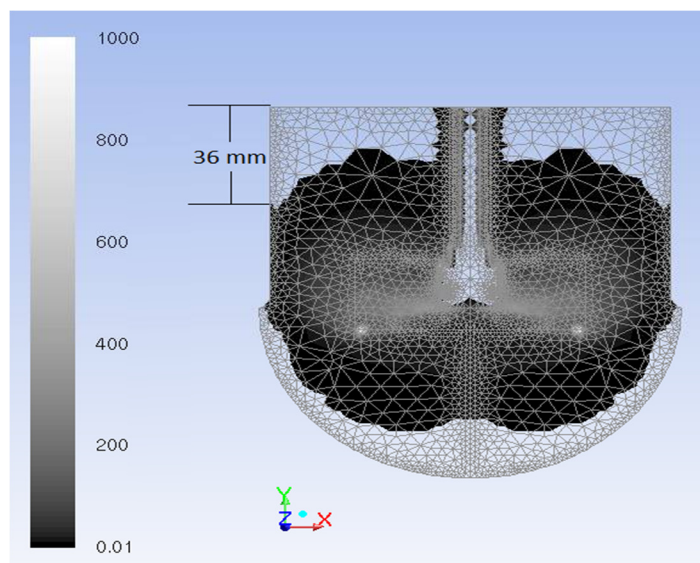
Figure 6.230: Cavern depth measured from CFD

at the tank wall. The depth was determined by measurement of where flow upwards along the wall stopped. The corresponding value in CFD was determined by where the local shear rate at the wall exceeded the critical shear rate (see Supporting Information). At 900 rpm, the experimental value was 38 mm, while simulation predicted 36 mm, a difference of 5 %. Below 900 rpm movement could not be observed at the wall, and above 900 rpm caverning was not consistently observed, since movement extended all the way to the top, which was consistent with CFD simulations.

6.3 EFFECT OF SCALE-UP ON POWER NUMBER FOR THE PBT

Fig. 6.3 shows the power number as a function of PV^{-1} and Re for the PBT. Across all impeller configurations, the simulated power number is 10–50 % (DT^{-1} = 1/3, CT^{-1} = 1/2, and DT^{-1} = 1/2, CT^{-1} = 1/2, respectively) of the Newtonian value of 1.5. The Reynolds transition for mixing tanks ranges from about 10 to 10 000. Both laminar and turbulent models were tested since the majority of cases operated in the transition region. All cases modeled with the RNG k-e turbulence model predicted P_0 results within 10 % of the laminar model, with an average difference of less than 4 %, for the full range of Reynolds numbers tested here. While turbulence models for cases in the low end of the transition region might be expected to produce results similar to the laminar model, the non-Newtonian slurry still behaves as though it were laminar at the higher end of the transition region, which differs significantly from Newtonian fluids that should behave closer to fully turbulent conditions at the higher end of the transition region. This is mostly attributed to the yield stress, which hinders motion for a certain amount of the fluid away from the impeller.
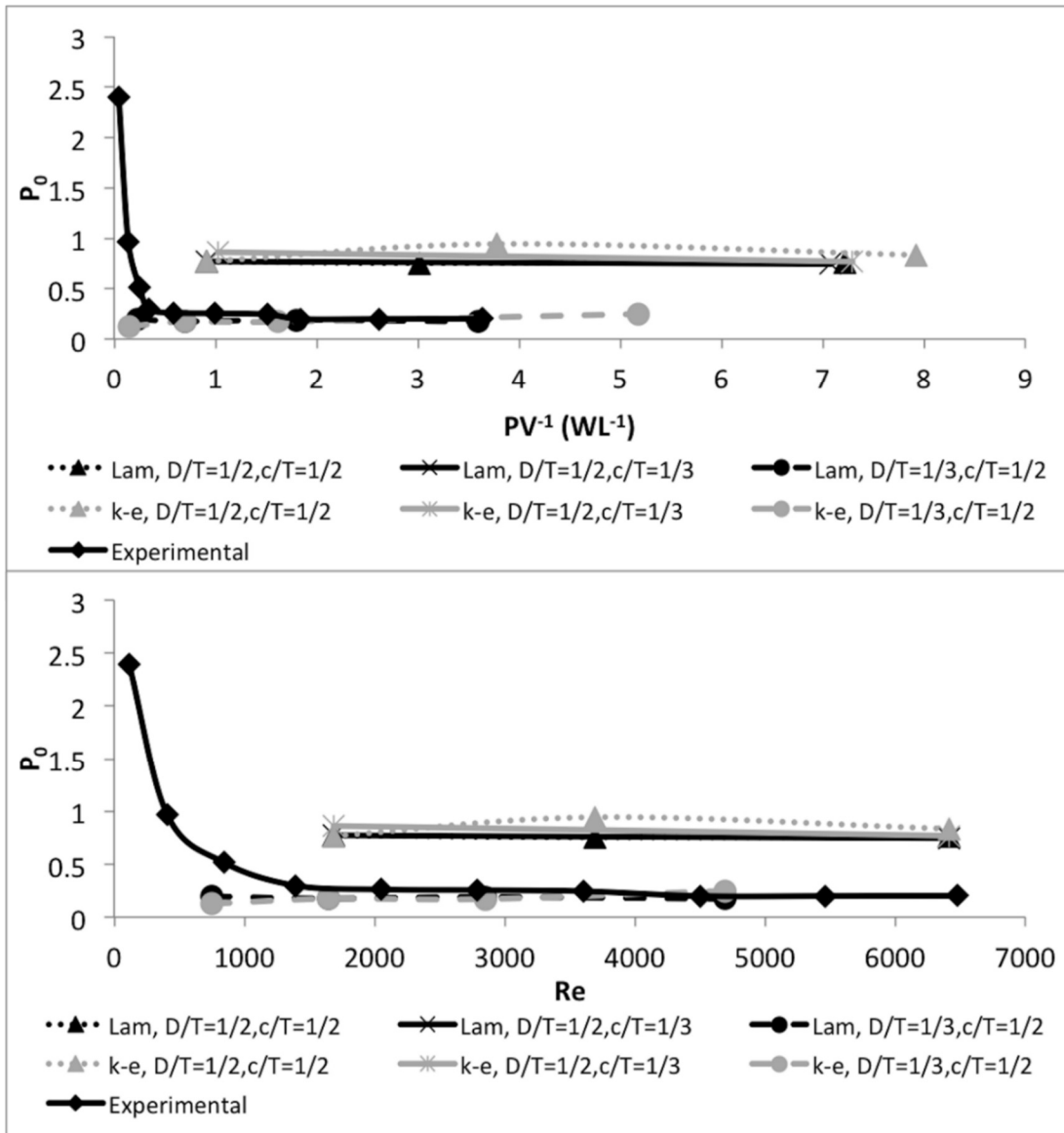
Figure 6.3: Simulated power number as a function of (a) PV⁻¹ and (b) Re for the PBT in the large-scale vessel. Data series ''Experimental'' is lab scale with DT⁻¹ = 1/2 and CT⁻¹ = 1/2.

6.4 PRESENCE OF TURBULENCE

Fig. 6.4 shows a comparison contour of turbulent and apparent viscosities. The
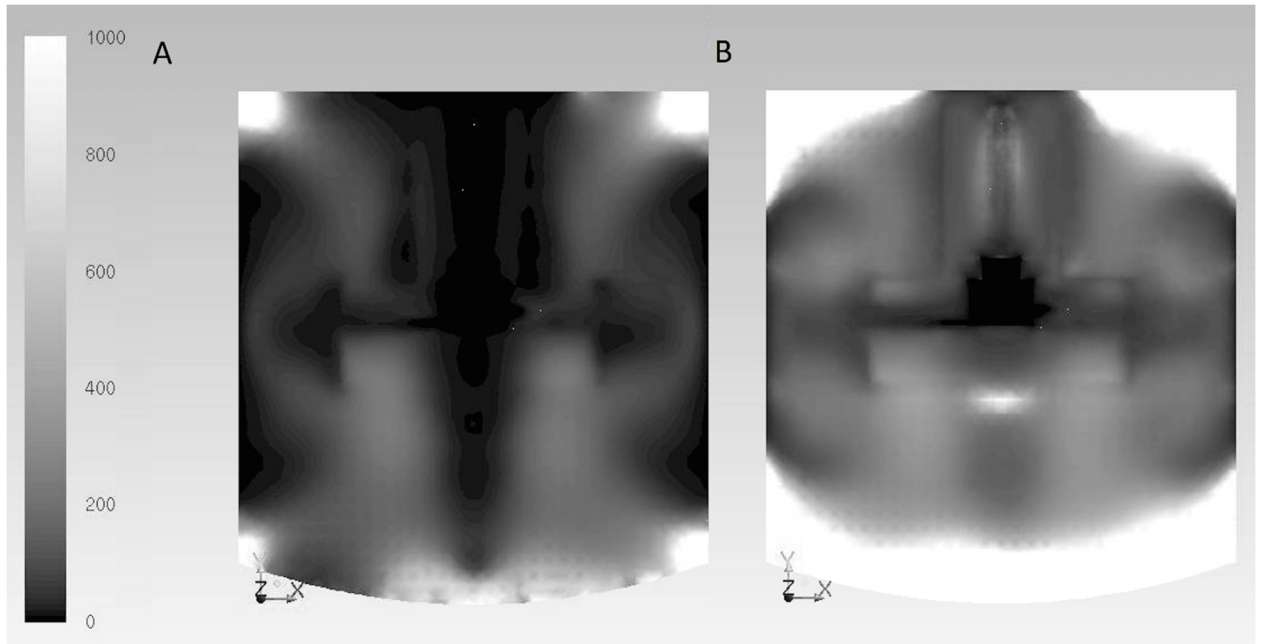
Figure 6.4: Comparison of (a) turbulent and (b) apparent viscosities for the PBT at 25 rpm, $DT^{-1} = 1/2$ and $CT^{-1} = 1/2$. Units are in kg $m^{-1}s^{-1}$.

apparent viscosity is much higher throughout most of the tank, indicating that turbulent

effects were less significant than rheology in this system. A fluid with a high yield stress

such as PCS slurries may never reach full turbulence. Further, the Reynolds numbers are

only estimated as per Metzner and Otto (1957), while Reynolds numbers will actually

vary across the tank as a function of shear. Consequently, a laminar model can be used to

simulate mixing in this system across this portion of the transition regime.

Figs. 6.2a and 6.2b show very similar trends. This indicates that PV^{-1} and

impeller speed track very closely with one another, and this relationship was not

significantly affected by changes in geometry. The large-scale system that maintains

geometric similitude with the small-scale setup, $DT^{-1} = 1/2$, $CT^{-1} = 1/2$, had a

significantly higher power number (0.75) than the lab scale system (0.25), indicating the substantial impact scale can have on the power number for a non-Newtonian system. Newtonian power numbers are constant irrespective of scale (Hemrajana & Tatterson, 2004). However, considering a volume scale factor of approximately 2 million produced a P0 change by a factor of 3, the effect is not that large. The amount of force required to overcome the yield stress in the PCS slurry is constant with distance from the impeller, meaning much more total energy is required at larger distances, while the shear thinning effect is dependent on the relative magnitudes of the non-uniform shear pattern throughout the vessel. Consequently, proportionally more energy is required from the impeller for the shear to propagate throughout the tank and overcome the yield stress. The interaction between these two factors explains the relatively small dependence of the power number on scale.

6.5 EFFECTS OF CHANGING GEOMETRIC ARRANGEMENT

Changing DT–1 did affect power draw and power number. Increasing DT^{-1} from 1/3 to 1/2 enlarged the power number by a factor of 3. Fig. 6.5 compares velocity vectors and shear rate patterns in these systems. Non-uniform shear patterns throughout the tank contribute to widely fluctuating rheology, which is exacerbated by scale. Changing the impeller diameter will alter the shear pattern, in that a larger portion of the tank will be in a higher shear environment. This is evident by the increase in motion away from the impeller for $DT^{-1} = 1/2$. The higher shear environment is more effective at overcoming the yield stress in laminar layers, such as in the center or well away from the main zones, which in turn will magnify the required power draw more so than it would for a Newtonian system, and consequently increase the power number.
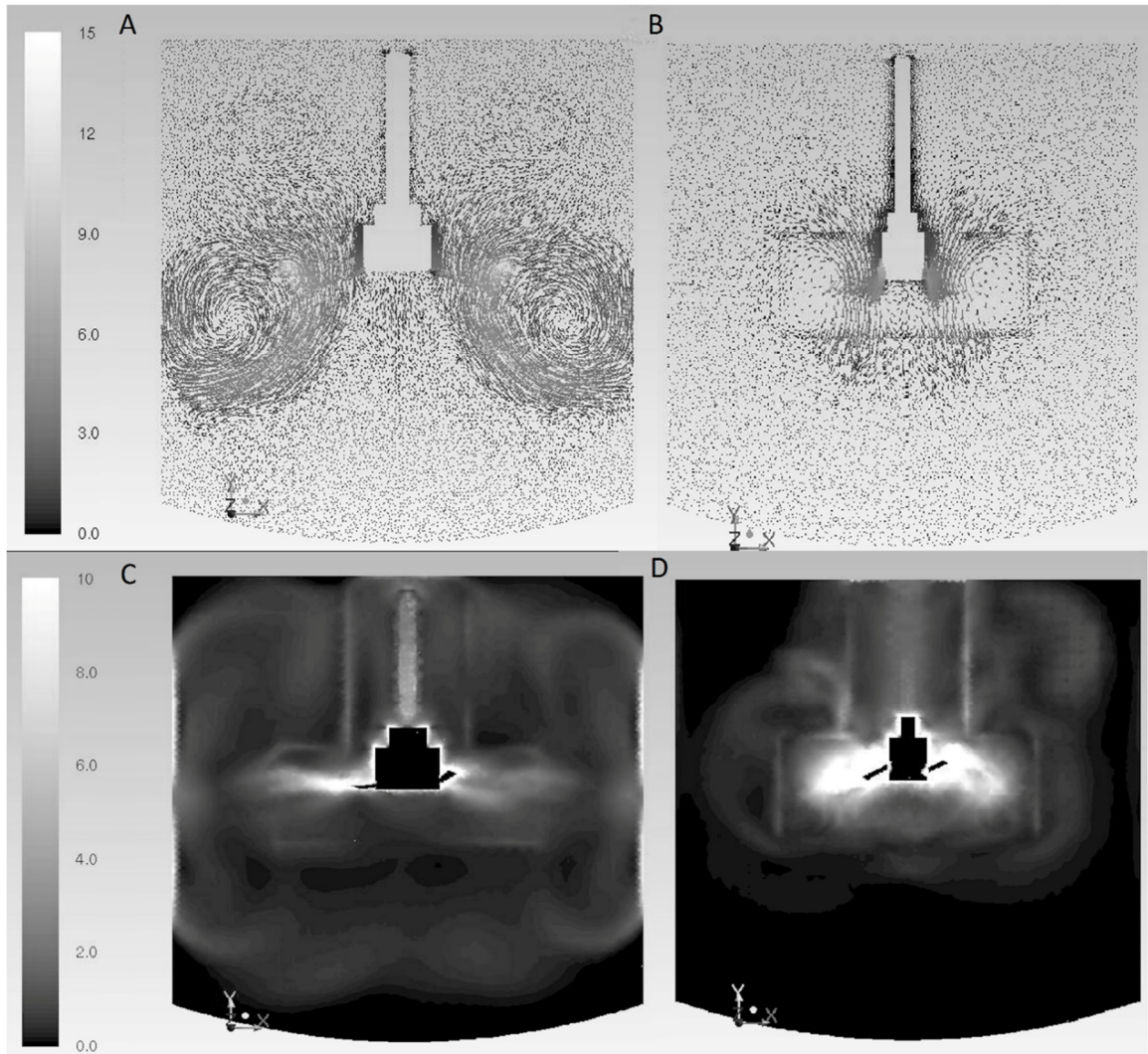
Figure 6.5: Comparison of velocity vectors for the PBT for (a) DT^{-1} = 1/2 and (b) DT^{-1} = 1/3 and shear rate contours (c) DT^{-1} = 1/2 and (d) DT^{-1} = 1/3. Units are in m s^{-1} (vectors) and s^{-1} (contours).

When comparing Fig. 6.4a to Fig. 6.5c, it is obvious that the turbulent viscosity becomes very high in unyielded regions of the vessel. High-viscosity regions (Fig. 6.4a) overlap with regions of lowest shear rate (Fig. 6.5c), indicating both predict the same dead zones.

For the PBT, changing CT^{-1} from 1/2 to 1/3 did not affect P_0. Within this range, the fluid path leaving the impeller blades was relatively unaffected by the clearance before turning near the wall. Fig. 6.6 shows the same shape for the main circulation loop
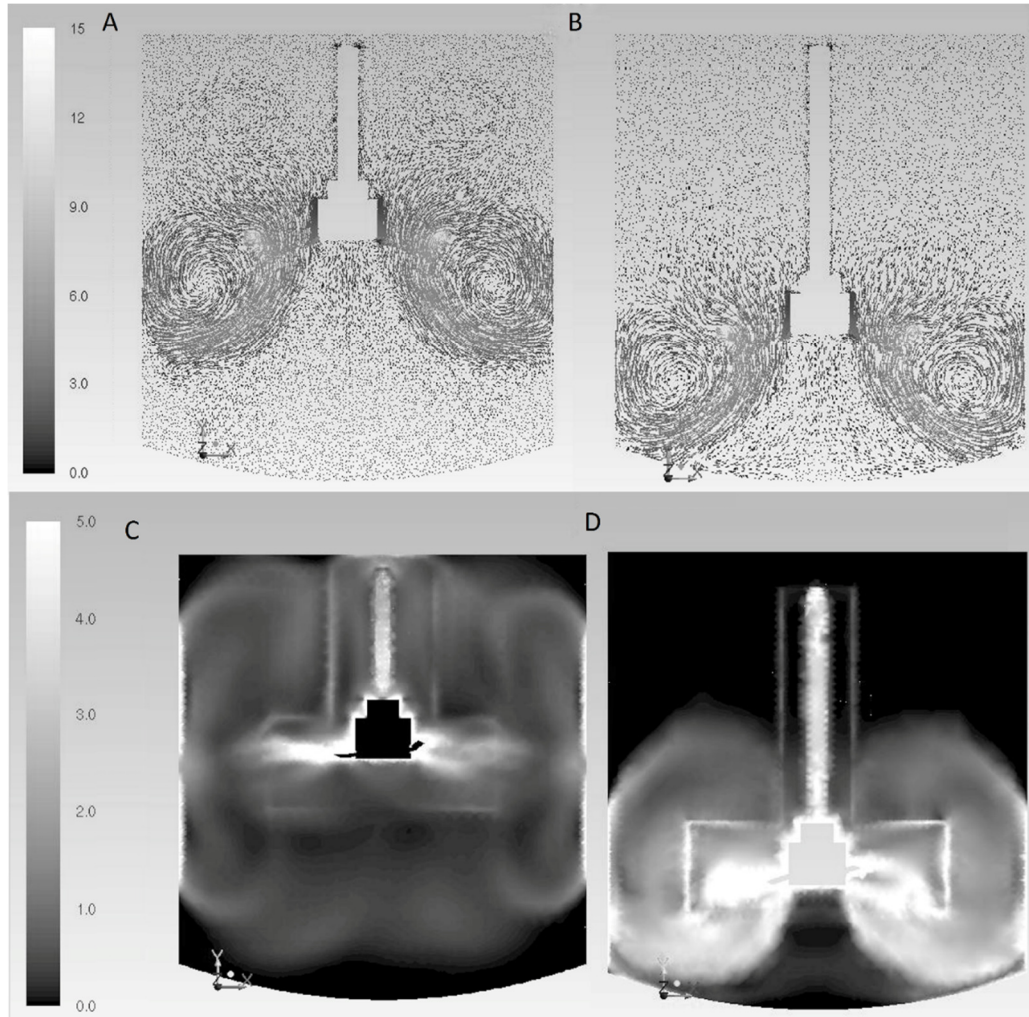
Figure 6.6: Comparison of velocity vectors for the PBT for (a) CT^{-1} = 1/2 and (b) CT^{-1} = 1/3 and shear rate contours (c) CT^{-1} = 1/2 and (d) CT^{-1} = 1/3. Units are in m s–1 (vectors) and s–1 (contours).

for either clearance. Clearance did not significantly affect the flow pattern. The shear pattern is very similar above the impellers, while below, the shear cannot spread as far, and so it is compressed into higher intensity instead. Therefore, the overall shear magnitude throughout the tank should be similar, since the smaller area below the

impeller is balanced by a greater intensity in the same region, and the corresponding

power number was not affected.

6.6 EFFECT OF SCALE-UP ON POWER NUMBER FOR THE HYDROFOIL IMPELLER

Results from the hydrofoil impeller (Fig. 6.7) were similar to the PBT, where the
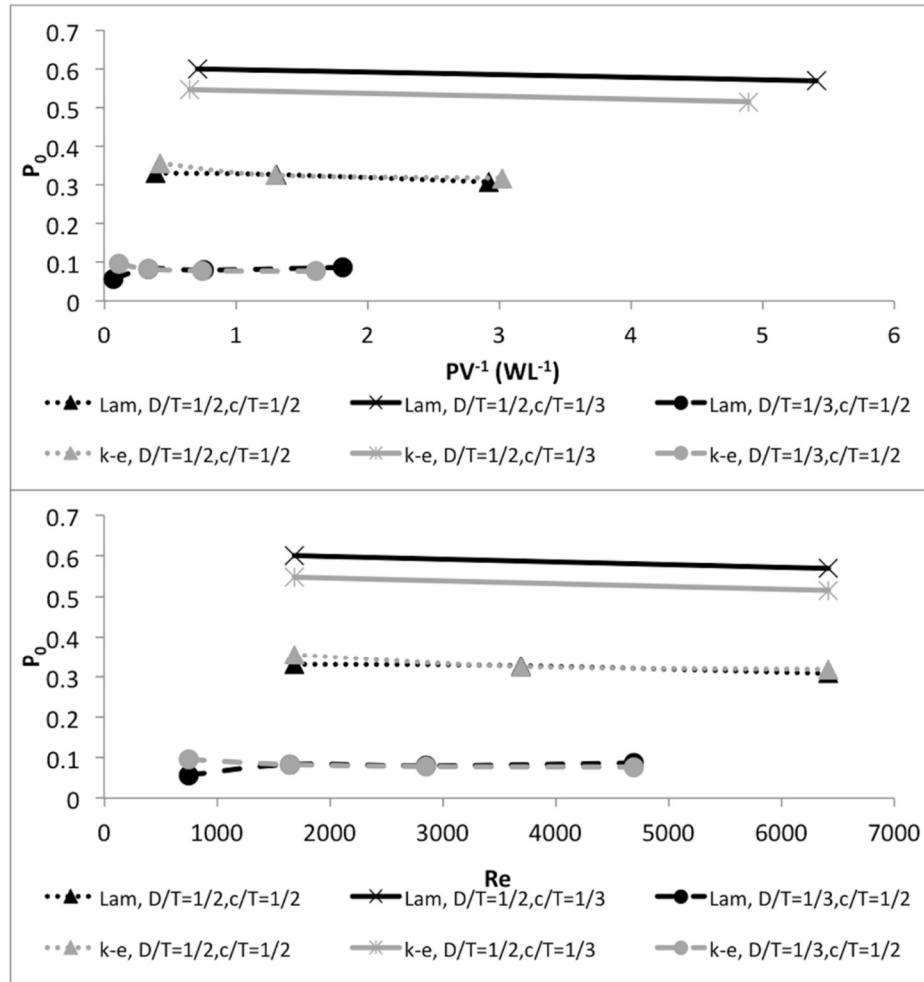
Figure 6.7: Simulated power number as a function of (a) PV^{-1} and (b) Re for the A310 in the full-size vessel.

laminar and turbulent models produced equivalent power numbers. For the hydrofoil, the

large-scale non-Newtonian P_0 values ranged 20–160 % ($DT^{-1} = 1/3$, $CT^{-1} = 1/2$ and DT^{-1}

$= 1/2$, $CT^{-1} = 1/3$, respectively) of the Newtonian value of 0.3. When comparing the

hydrofoil with the PBT, for Newtonian systems, the ratio between the hydrofoil and the

PBT power numbers was 1:5. However, in the large-scale non-Newtonian system, the ratio for the $DT^{-1} = 1/2$, $CT^{-1} = 1/2$ system was 1:2.5. This implies that the PBT is more sensitive of the effects of the non-Newtonian rheology than is the hydrofoil.

Again, similarly to the PBT, increasing DT–1 from 1/3 to 1/2 increased P_0 by about a factor of 4. This maintains the same A310:PBT ratio of 1:2.5 across both impeller sizes. As with the PBT, this is due to changing shear patterns throughout the tank, which magnify the power changes because of the non-Newtonian rheology. The larger impeller will create higher shear throughout a larger portion of the tank, which means more energy must be spent overcoming the yield stress.

Unlike the PBT, changing CT–1 affects P0 for the hydrofoil. Changing from 1/2 to 1/3 increases P_0 by approximately 60 % (A310:PBT is 1:1.5). The difference between the hydrofoil and the PBT in this respect is probably due to the differing flow patterns created by the two impellers. The A310 produces a more axial flow, with less of a radial component, than the PBT. Thus, the A310 is more sensitive to the proximity of the vessel bottom as it redirects the flow leaving the impeller. In the non-Newtonian environment, this effect is going to be magnified, since rapid change in flow direction requires additional energy to overcome the yield stress, and, therefore, the power draw will be more sensitive to it.

Targets for PV^{-1} input at industrial scale are typically in the range of 1–5 W L^{-1} (Arjunwadker et al, 1998). Across the range tested here, PV^{-1} extended both above and below this range. The predicted power numbers for the PBT impeller resulted in PV–1 as high as 16 W L^{-1} for $DT^{-1} = 1/2$, $CT^{-1} = 1/3$. The hydrofoil, with lower power numbers operated at the lower end of that range, e.g., 0.1–1.5 WL^{-1} for the $DT^{-1} = 1/3$, $CT^{-1} = 1/2$

cases, but still requires 2–10 MW of power. Given the large vessel size and corresponding high power requirements, operating at high solids may be prohibitive at this scale.

6.7 SUMMARY

A CFD model was developed to predict power requirements of non-Newtonian high-solids lignocellulosic slurry in a 3.8-million-L hydrolysis reactor. First, a lab-scale model was well validated against experimental data by comparing torque to turn the impeller shaft. The model was then scaled up to 3.8 million L, which represents a hypothetical industrial-scale reactor for performing enzymatic hydrolysis. On this scale, a pitched-blade turbine and an A310 hydrofoil were tested with different impeller diameters, clearances, and speeds. For this yield stress fluid, enlarging the scale by a factor of 2 million led to an increase in power number by a factor of 3. For both impellers, increasing DT^{-1} from 1/3 to 1/2 raised the power number by a factor of 3. Changing impeller clearance did not affect P_0 for the PBT, but reduced clearance did significantly increase P_0 for the hydrofoil impeller. Since Reynolds numbers indicated that the flow was in the transitional region, a laminar model and RNG k-e model were both tested and yielded the same P_0 values. Finally, a vessel of this size can be expected to draw 2–10 MW of power under the most efficient conditions tested, indicating high-solids enzymatic hydrolysis in a conventional reactor at this scale may not be feasible.

CHAPTER 7. CONCLUSIONS

The theme of this dissertation was to evaluate mixing of individual phases independent of each other in multiphase systems through application of mean age theory. The work was divided into three sections. The first dealt with extending existing mean age theory for single phase systems to multiphase systems. Secondly, mean age theory, which was developed for open flow systems, was modified here for closed systems, and then applied towards predicting just suspended speed in liquid-solid suspensions. Lastly, the effect of rheology and scale on power requirements and mixing quality in high solids biomass slurries was studied.

A new theory was developed for determining spatial and temporal mean age distributions for each phase independently in multiphase systems. The theory requires defining the concentration of a passive scalar in terms of the density and volume fraction for each phase at every location over time. The theory was well validated against experimental data by simulating mean age distributions for water-oil flow in a pipeline. Mean residence times generated computationally by MMA theory were within 1% of experimental values for the primary water phase and 3% for the secondary oil phase. MMA curve variances differed by 3-11% between the computational and experimental RTD results. Means and variances of the new steady-state MMA method matched experimental values more closely than did the conventional transient computations, indicating better accuracy when using the steady-state solution. MMA theory provides a substantial improvement over traditional RTDs since it provides age distributions over

space and volume rather than just at discrete locations, plus it is more computationally practical for applications with very long time scales. The technique demonstrated versatility with application to both liquid-liquid and liquid-solid multiphase systems, and should be easily extendable to systems involving gas phases as well, allowing for a wide variety of applications including pollution modeling, fluidized beds, sedimentation modeling, and cardiovascular applications, among many others.

This new MMA theory was applied towards accurately predicting the just suspended speed in mixing tanks. A closed system with modified boundaries generated results as reliably as the rigorous open system. The multiphase mean age technique was shown to accurately predict N_{jss} across a range of solid densities, solid fractions, and particle sizes with average deviation from published experimental data of just 1-3%. Furthermore, tests were performed in different size tanks with different impeller types indicating accuracy across a range of scale and geometries. This steady state CFD technique can predict just suspended speed results with less computational time compared to unsteady CFD methods, with error equivalent to experimental methods, and without inherent experimental drawbacks such as altering the flow regime, requiring transparency, or subjective experimental variability.

In high solids conditions, a CFD model was developed to predict power requirements of non-Newtonian lignocellulosic slurry in a 3.8-million-L hydrolysis reactor. First, a lab-scale model was well validated against experimental data by comparing torque to turn the impeller shaft. The model was then scaled up to 3.8 million L, which represents a hypothetical industrial-scale reactor for performing enzymatic hydrolysis. On this scale, a pitched-blade turbine and an A310 hydrofoil were tested with

different impeller diameters, clearances, and speeds. For this yield stress fluid, enlarging the scale by a factor of two million led to an increase in power number by a factor of three. For both impellers, increasing DT^{-1} from 1/3 to 1/2 raised the power number by a factor of three. Changing impeller clearance did not affect P_0 for the PBT, but reduced clearance did significantly increase P_0 for the hydrofoil impeller. Since Reynolds numbers indicated that the flow was in the transitional region, a laminar model and RNG k-e model were both tested and yielded the same P_0 values. Finally, a vessel of this size can be expected to draw 2–10 MW of power under the most efficient conditions tested, indicating high-solids enzymatic hydrolysis in a conventional reactor at this scale may not be feasible.

CHAPTER 8. RECOMMENDATIONS

This study could be extended by studying more thoroughly the relationship between multiphase mean age distributions and residence time distributions. In a perfectly plug flow scenario, these two should be identical, but the more mixing occurs, the greater the deviations would be. Since the multiphase mean age solution is averaged, the distribution will tend to be somewhat narrower than the residence time distribution. The wider the RTD, the more pronounced this effect will be. This study could be accomplished by simulating several systems with progressively greater levels of mixing. A yield stress fluid flowing through a pipe at low velocity (true plug flow), a Newtonian fluid in laminar conditions, a Newtonian fluid flowing in highly turbulent conditions, and a highly turbulent, Newtonian fluid flowing through a pipe with added inline mixers and recirculation lines. Each of these conditions would be progressively more mixed than the previous. Each system could be studied by comparing the multiphase mean age distribution obtained from a steady state CFD solution to an unsteady state CFD solution with a passive tracer. Further information could be learned by individually adjusting the viscosity and concentration of each phase, so that one phase is significantly more mixed than the other.

Another extension could be to apply the mean age concepts to the high solids biomass slurries. Those systems are currently being studied extensively, due to the common research emphasis on biofuels. Using mean age to study these non-Newtonian

slurries could provide insight as to their mixing quality, and could be related to the mass transfer involved with the reaction. Further extension could be to directly relate the age scalar concept with reaction progress in these systems. Since the reaction occurs on a time scale determined by predictable kinetics, it is feasible to devise a scheme in which mean age is calculated in proximity to unreacted substrate (as it moves about the vessel). This new scalar would directly predict the steady state reaction progress throughout a vessel. It would more readily identify mixing problems as they pertain to the process yield. This could be accomplished by tracking a passive scalar contained within the substrate. Such a scalar would have a modified source term. Rather than a constant value representing the passage of time, this scalar would increase or decrease in value based on the local enzyme concentration. To build the model, well mixed reaction rate data would need to be obtained for a variety of enzyme-substrate ratios. Then the same system could be modelled with CFD. The output scalar value would be correlated to the reaction yield in laboratory, so that a reliable correspondence between the two is made. For a more robust outcome, the rheology of the slurry at various points of reaction progress could be measured. Then the prediction of reaction yield could be coupled with the rheology of the slurry within the CFD model, enhancing the predicted result. This concept, if successful, could become the gold standard for CFD modelling the mixing of reactive processes, since the most important outcomes in these systems are reaction progress and power draw. This application would tie together and apply all three objectives of this work (multiphase mean age, age in proximity to small portions of a vessel, mixing in high solids biomass slurries).

REFERENCES

1. A, Aden, M. Ruth, K. Ibsen, J. Jechura, K. Neeves, J. Sheehan, B. Wallace (National Renewable Energy Laboratory, Golden, CO), L. Montague, A. Slayton, J. Lukas (Harris Group, Seattle, WA), Lignocellulosic biomass to ethanol process design and economics utilizing co-current dilute acid prehydrolysis and enzymatic hydrolysis for corn stover. Golden (CO): National Renewable Energy Laboratory (US); 2002 Jun. 88 p. Report No.: NREL/TP-510-32438.

2. S. Arjunwadker, K. Saravan, A. Pandit, P. Kulkarni, *Biochem. Eng. J.* **1998**, 1 (1), 25-30 DOI: 10.1016/S1369-703X(97)00005-3

3. P. Armenante, E. Nagamine, J. Susanto, *Canad J Chem Eng.* 1998, 76, 413-419

4. A. Bakker *Applied computational fluid dynamics* **2006** http://www.bakker.org/dartmouth06/engs150/10-rans.pdf

5. J. Baleo, P. Cloirec, *AICHE J.* **2000** 46, 675-683

6. A. Bartosik, *Flow, Turbul. and Combust.* **2010**, 84 (2), 277-293 DOI: 10.1007/s10494-009-9234-y

7. W. Bujalski, K. Takenaka, S. Paolini, M. Jahoda, A. Paglianti, A. Takahashi, A.W. Nienow, A.W. Etchells, *Trans. IChemE* **1999**,77 (A), 241-247

8. C. Buurman, G. Resoort, A. Plaschkes *Chem Eng Sci*. **1986**, 41, 2865-2871

9. C. Chapman, A. Nienow, M. Cooke, J. Middleton. *Chem Eng Res Des.* 1983, 61, 71-81

10. P. Danckwerts. *Chem Eng Sci*. **1953**, 2, 1-13

11. P.V. Danckwerts. *Chem Eng Sci.* **1958**, 8, 93–102.

12. R.K. Dasari, K.W. Dunaway, R.E. Berson, *Energy Fuels* **2009**, 23, 492-497 DOI: 10.1021/ef800434u

13. S.E. Desouky, M.N. Al-Awad, *J. Pet. Sci. Eng.* **1998**, 19 (3-4), 171-176 DOI: 10.1016/S0920-4105(97)00044-2

14. K.W. Dunaway, R.K. Dasari, N.G. Bennett, R.E. Berson, *Bioresour. Technol.* **2010**, 101 (10), 3575-3582 DOI: 10.1016/j.biortech.2009.12.071

15. J. Ding, D. Gidaspow, *AICHE J.* **1990**;36:523-538

16. W. Einenkel, A. Mersmann, *Verfahrenstechnik.* **1977,** 11, 90-94.

17. G.F. Froment, K.B Bischoff. *Chemical reactor analysis and design.* New York: John Wiley & Sons, Inc.; 1979

18. R.A. Ghotli, A.A. Raman, S. Ibrahim, S. Baroutian, *Chem. Eng. Commun.* **2013**, 2005 (5), 595-627

19. Y. Guntzberger, A. Fontaine, L. Fradette, F. Bertrand, *Chem Eng J* **2013**, 214, 394-406 DOI: 10.1016/j.cej.2012.10.041

20. R.R. Hemrajana, G.B. Tatterson, in *Handbook of Industrial Mixing – Science and Practice*, (Eds E. L. Paul, A.V. Atiemo-Obeng, and S.M. Kresta), Wiley-Interscience, Hoboken, NJ **2004**

21. Y. Hirata, Y. Aoshima, *Trans. IChemE* **1996**, 74 (A), 438-444

22. M. Liu, *Canad J Chem Eng.* **2011,** 89, 1018-1028

23. M. Liu, J. Tilton, *AICHE J.* **2010**, 56, 2561-2572.

24. C.K.K. Lun, S.B. Savage, D.J. Jeffrey, N. Chepurniy, *J Fluid Mech.* **1984,** 140, 223-256

25. M.R. Malin, *Int. Commun. Heat Mass Transfer* **1998**, 25 (3), 321-330 DOI: 10.1016/S0735-1933(98)00019-0

26. A.B. Metzner, J.C. Reed, *AICHE J.* **1955**, 1 (4), 434-440 DOI: 10.1002/aic.690010409

27. A.B. Metzner, R.E. Otto, *AICHE J.* **1957**, 3 (1), 3-10 DOI: 10.1002/aic.690030103

28. G. Micale, V. Carrara, F. Grisafi, A. Brucato, *Chem Eng Res Des.* **2002**, 80, 893-902.

29. L. Musil, J. Vik, *Chem Eng Sci.* **1978,** 33, 1123-1131.

30. A.W. Nienow, T.P. Elson, *Chem. Eng. Res. Des.* **1988**, 66 (1), 5-15

31. J.M. Nouri, R.M. Hockey, *J. Chem. Eng. Jpn.* **1998**, 31 (5), 848-852 DOI: 10.1252/jcej.31.848

32. J.Y. Oldshue *Fluid mixing technology*, 1st ed, McGraw-Hill, New York (1983)

33. D.J. Patil, M.V. Annaland, J.A.M. Kuipers, *Intl J Chem Reactor Eng.* **2003,** 1

34. E. Paul, V. Atiemo-Obeng, S. Kresta, Introduction. In E. Paul, V. Atiemo-Obeng, S. Kresta, *Handbook of industrial mixing: Science and practice.* Hoboken, NJ: John Wiley & Sons, Inc. **2004**

35. J. Peixinho, C. Nour, C. Desaubry, B. Theron, *J. Non-Newtonian Fluid Mech.* **2005**, 128 (2-3), 172-184 DOI: 10.1016/j.jnnfm.2005.03.008

36. N.V. Pimenova, T.R. Hanley, *Appl. Biochem. Biotechnol.* **2004**, 114 (1-3), 346

37. K. Rao, V. Rewatkar, J. Joshi, *AIChE J.* **1988,** 34, 1332-1340

38. M.L. Samano, A. Garcia, J.A. Revilla, C. Alvarez, *Environ Earth Sci.* **2014,** 72, 2931-2945

39. M. Sandberg, *Build Environ.* **1981,** 16, 123-135

40. A. Sarkar, W. Pan, D.M. Suh, E.D. Huckaby, X. Sun, *Powder Tech.* **2014,** 265, 35-46

41. X. Shao, L. Lynd, A. Bakker, *Bioprocess Biosyst. Eng.* **2010**, 33 (4), 485-493 DOI: s00449-009-0357-2

42. A.J. Sinusas, J. Lazewatsky, J. Brunetti, *J Nucl Med.* **2014,** 55, 1445-1451

43. D.B. Spalding, *Chem Eng Sci.* **1958**, 9, 74-77

44. J.J. Stickel, J.S. Knutsen, M.W. Liberatore, W. Luu, D.W .Bousfield, D.J. Kingenberg, C.T Scott, T.W. Root, M.R. Ehrhardt, T.O Monz, *Rheol. Acta* **2009**, 48 (9), 1005-1015 DOI: 10.1007/s00397-009-0382-8

45. S. Sugiharto, Z. Su'ud, R. Kurniadi, *Applied Radiation Isotopes.* **2009,** 67, 1445-1448

46. M. Syamlal, T.J. Obrien, *Intl J Multiphase Flow.* **1989**, 14, 473-481

47. M. Tambasco, D.A. Steinman, *J Biochem Eng.* **2002**, 124, (2), 166-175.

48. G.B. Tatterson, R. Calabrese, W.R. Penney, *Industrial mixing technology: chemical and biological applications*, 1st ed., American Society of Chemical Engineers, New York **1994**

49. P.C. Wang, X.Q. Zhang, Q. Zao, M.Z. Shi, *J Hydrodynamics*. **2013**, 25, 39-47

50. R.J. Wilkens, C. Henry, L.E. Gates, *Chem. Eng. Prog.* **2003**, 99 (5), 44-52

51. B. Wu, *Biotechnol. Bioeng.* **2012**,109 (3), 804-812 DOI: *10.1002/bit.24345*

52. B. Wu, S. Chen, *Biotechnol. Bioeng.* **2008**, 99 (3), 700-711 DOI: 10.1002/bit.21613

53. T. Zwietering, *Chem Eng Sci*. **1958**, 8, 244-258.

APPENDIX I. USER DEFINED FUNCTION

Below is a user defined function for use in Fluent. In some multiphase problems,

the volume fraction of the secondary phase is not conserved. This UDF will correct the

volume fraction to the specified value before each iteration, ensuring that the target

volume fraction is maintained.

```
#include "udf.h"
#include "sg_mphase.h"
#include "sg.h"
#include <stdio.h>
#define pi 4.*atan(1.)

/* ********************************************************** */
/* This UDF fixes the overall volume fraction of the        */
/* granular phase to a user specified value. To function    */
/* properly, the user should first read the SCHEME file     */
/* "granpar.scm" before reading case and data. This creates */
/* an input panel DEFINE | GRANULAR DRAG AND VOLUME FRACTION */
*/
/* The user specifies the necessary inputs there.           */
/*                                                          */
/*                                                          */
/* ********************************************************** */

/* ********************************************************** */
/* UDF for fixing the volume fraction of the granular phase  */
/* ********************************************************** */

DEFINE_ADJUST(fix_gran_vf, domain)
{
 Thread *t;
 Thread **pt;
 int doprint = 1;
 int gphase = 2 - 1;
 real targetvf = 0.05;   /*change this one*/
 real vof_max =
```

```
DOMAIN_PROP_CONSTANT(DOMAIN_SUB_DOMAIN(domain,gphase),PR
OP_packing) - 1.e-3;
  real vof_max2 =

DOMAIN_PROP_CONSTANT(DOMAIN_SUB_DOMAIN(domain,gphase),PR
OP_packing) - 1.e-2;
 real packvolume;
 real notpackvolume;
 real totvolume;
 real multiplier;
 real deltavof;

 packvolume = 0.0;
 notpackvolume = 0.0;
 totvolume = 0.0;

 /* loop over domain */
 mp_thread_loop_c (t,domain,pt)
  if (FLUID_THREAD_P(t))
   {
       cell_t  c;
       begin_c_loop_int (c,t)
        {
         real c_vol = C_VOLUME(c,t);
       totvolume += c_vol;
         if (C_VOF(c,pt[gphase]) > vof_max2)
           {
              packvolume += C_VOF(c,pt[gphase])*c_vol;
           }
       else
        {
         notpackvolume += C_VOF(c,pt[gphase])*c_vol;
        }

        }
       end_c_loop_int (c,t)
    }
/*ensure all compute nodes have the same summation values for parallel
calculations */
#if RP_NODE
   totvolume=PRF_GRSUM1(totvolume);
       packvolume=PRF_GRSUM1(packvolume);
   notpackvolume=PRF_GRSUM1(notpackvolume);
#endif
 /*end loop over domain */
```

```
/* execute rest only if totvolume>0, otherwise the      */
/* routine was called from the compute host in parallel */

if (totvolume>0)
{

  multiplier=(targetvf*totvolume-packvolume)/notpackvolume;
  if (multiplier<1.0)
multiplier=(targetvf*totvolume)/(packvolume+notpackvolume);
  if (multiplier>1.0) multiplier=(multiplier-1)*.75 + 1;
  if (multiplier<1.0) multiplier=1-(1-multiplier)*.75;
  if (doprint>0)
  {
   Message ("mass correction factor = %8.6g\n",multiplier);
    Message ("");
  }

  if (multiplier<1.0)
  {
  mp_thread_loop_c (t,domain,pt)
   if (FLUID_THREAD_P(t))
    {
        cell_t  c;

        begin_c_loop_int (c,t)
         {
                deltavof = C_VOF(c,pt[gphase]) * multiplier;
           deltavof -= C_VOF(c,pt[gphase]);
           C_VOF(c,pt[gphase]) += deltavof;
           C_VOF(c,pt[0]) -= deltavof;
         }
        end_c_loop_int (c,t)
    }
  }
  else
  {
  mp_thread_loop_c (t,domain,pt)
   if (FLUID_THREAD_P(t))
    {
        cell_t  c;

        begin_c_loop_int (c,t)
         {
           if (C_VOF(c,pt[gphase]) < vof_max2)
            {
```

110

```
            deltavof = C_VOF(c,pt[gphase]) * multiplier;
        if (deltavof > vof_max) deltavof=vof_max;
        deltavof -= C_VOF(c,pt[gphase]);
        C_VOF(c,pt[gphase]) += deltavof;
        C_VOF(c,pt[0]) -= deltavof;
          }
      }
    end_c_loop_int (c,t)
  }
 }
 }
}
```

CURRICULUM VITAE

NAME: David Chandler Russ

ADDRESS: 33604 Bostwick Pl
            Farmington Hills, MI 48335

DOB: Winston-Salem, North Carolina – October 24, 1987

EDUCATION
& TRAINING: B.S., Chemical Engineering
                     University of Louisville
                     2006-2010

                     M.Eng., Chemical Engineering
                     University of Louisville
                     2010-2011

                     Ph.D., Chemical Engineering
                     University of Louisville
                     2011-2016

AWARDS: University Fellowship 2011-2013

PROFESSIONAL SOCIETIES: American Institute of Chemical Engineers

                               Tau Beta Pi

PUBLICATIONS:

                     Russ, D., Thomas, J., Miller, Q., & Berson, R. (2014). Predicting
                     Power for a Scaled-up Non-Newtonian Biomass Slurry. *Chemical
                     Engineering & Technology*, 38(1), 53-60.
                     doi:10.1002/ceat.201400327

                     Russ, D., & Berson, R. (2016). Mean Age Theory for Multiphase
                     Systems. *Chemical Engineering Science*, 141, 1-7.

                     Ghorbanian, M., Russ, D., & Berson, R. (2014). Mixing analysis of
                     PCS slurries in horizontal scraped surface bioreactor. *Bioprocess*

& Biosystems Engineering 37(10), 2113-2119.
doi:10.1007/s00449-014-1189-2

NATIONAL MEETING PRESENTATIONS:

Steady State CFD for Determining Just Suspended Speed
American Institute of Chemical Engineers Annual Meeting 2013
November 6, 2013
San Francisco, California

Mean Age and Just Suspended Speed in Multiphase Mixtures
American Institute of Chemical Engineers Annual Meeting 2014
November 18, 2014
Atlanta, Georgia
Mean Age in Multiphase Systems
American Institute of Chemical Engineers Annual Meeting 2015
November 10, 2015
Salt Lake City, Utah